Environment-organism feedbacks drive changes in ecological interactions

Oliver J. Meacock *[1] and Sara Mitri [1]

[1]Department of Fundamental Microbiology, University of Lausanne, Lausanne, Switzerland

Abstract

Ecological interactions, the impact of one organism on the growth and death of another, underpin our understanding of the long-term composition and the functional properties of communities. Interactions from classical ecology are typically understood to be fixed values, representing for example the per-capita consumption rate of prey by its predator. Yet in many ecosystems, such fixed descriptions are inadequate: interactions can depend on local environmental conditions, the time at which they are measured, and the sampled position in a spatially-structured community. In this work, we show that each of these three types of context-dependency can arise from feedbacks between organisms and their environment. At the heart of our theory is the 'instantaneous interaction', a quantity that describes whether a given population changes their surroundings in a way that helps or hinders another in a particular environment. This environmentally-dependent quantity then gives rise to time and spatial dependencies as the environment changes over time and/or space. We use small synthetic microbial communities as model ecosystems to demonstrate the power of this framework by showing how we can predict time-dependent intra-specific interactions, and how we can relate time and spatial dependencies in crossfeeding communities. Our framework helps to explain the ubiquity of interaction context-dependencies in systems where population changes are driven by environmental changes – such as microbial communities – by placing the environment on an equal theoretical footing as the organisms that inhabit it.

Keywords: Ecological interactions, consumer-resource modelling, microbial communities

*oliver.meacock@unil.ch

1 Introduction

Interactions between organisms - the impact of one species on the fitness or growth rate of another[1,2] - are one of the most consistent themes in ecology. One reason for this is that they are a key component of ecological models which provide testable predictions of community co-existence outcomes.[3,4] Though classically used to explore macroscopic ecosystems such as foodwebs,[5] in recent years interaction-based frameworks have also become a subject of deep study among microbial ecologists as a means of rationally manipulating community composition and function.[6,7]

Experimentally, the gold standard for estimating microbial interactions *in vitro* is to culture a focal species alone and in co-culture with another species and then compare the resulting growth of the focal species between the two conditions.[8–13] While the precise measurement defined as the 'interaction' varies from study to study,[14,15] in each case these experiments assign a single value to the interaction between pairs of species (the inter-specific interaction) or within the population of a single species (the intra-specific interaction). These can then be inserted into a theoretical model of population dynamics which can in turn be used to predict community properties, with the generalised Lotka-Volterra (gLV) framework being among the most popular choices.[7,9]

However, microbes do not typically interact via the direct, trophic mechanisms which the Lotka-Volterra framework was originally built to describe. Instead, microbial interactions are often mediated indirectly via abiotic intermediaries secreted into and taken up from the environment,[16] such as crossfed nutrients[17,18] and toxic compounds used to kill competitors.[19] Consumer-Resource models explicitly describe such mechanistic feedbacks between environmental resources and consuming species, and are widespread in classical ecology.[20,21] More recently, this framework has been extended to encompass secretion and toxicity of intermediates,[22] which we will refer to as the Environment-Organism (EO) framework. Comparisons between gLV and EO models have begun to reveal dynamical behaviours of EO systems that cannot be captured by direct, gLV-type interactions.[23] At the same time, experimental evidence has begun to accumulate showing that properties of microbial communities cannot necessarily be predicted from measurements of pairwise species combinations as the gLV framework would suggest.[24,25]

Context dependencies of interactions have become increasingly apparent as one explanation for this breakdown.[1,14,26] Specifically, interactions can vary depending on the chemical environment in which they are measured[11,27–31] and the time at which they are measured,[32,33] and spatial structure in multi-species communities is at least qualitatively understood to influence inter-species interactions.[34] These observations substantially complicate the fixed-interaction view that has typically been adopted by theoreticians, and present a substantial barrier to a general understanding of the properties of microbial communities and to our ability to predict their behaviour. Breaking down this barrier relies on understanding whether interactions change in predictable ways.

In this manuscript, we approach this problem by building a formal theoretical framework for understanding interaction context dependencies in EO systems. First, we show how a quantity we call the 'instantaneous interaction' – the environmentally-dependent effect that one species has on the growth of another given the local concentrations of different intermediates – arises naturally out of the fundamental equations describing EO systems. This instantaneous interaction accumulates as the chemical environment of the system is gradually modified by the community. Communities in closed systems without influx or efflux of intermediates sweep out trajectories in the space of possible environments over time or space, and this changing environmental context leads to *predictable* variations in the instantaneous interaction. In the most dramatic cases, this can lead to switching of the sign of interactions, from positive to negative or vice versa. We then verify these predictions by measuring time-dependent interactions in an experimental model based on antibiotic degradation. Finally, we show how time dependencies and certain types of spatial dependency can both be explained as arising from a single set of processes, theoretically unifying the observations of two recent studies[33,35] on time and spatial interaction dependencies in small crossfeeding communities. Our work demonstrates that the context dependencies so often observed in microbial ecosystems are an inevitable consequence of the mechanistic basis for most microbial interactions, the feedback between microbes and their environment.

2 Results

2.1 A theoretical Environment-Organism interaction framework explains multiple context-dependencies

We begin by considering general EO systems for which complex metabolic interactions can be decomposed into elementary components, each mediated by a single intermediate. Our goal will be to write a general expression for population dynamics containing an interaction term, analogous to the measurable interaction term of gLV systems but explicitly mediated by the dynamics of the intermediates. This will provide a direct link between the environmental context of the system and the measured microbial interactions.

EO systems can be modelled by breaking them into two distinct parts:[21,22,36] firstly the *impact function* of a species β, $\boldsymbol{f}_\beta(\boldsymbol{r})$ describes the rate at which one unit of β modifies its chemical environment. We denote this environment with the vector $\boldsymbol{r}$, which we will restrict as representing the concentrations of different intermediates (*e.g.* element 1 represents the concentration of glucose, while element 2 represents the concentration of acetate). $\boldsymbol{r}$ defines a position in the 'environment space', the set of different possible combinations of concentrations of intermediates. The impact function is itself dependent upon $\boldsymbol{r}$, allowing it to capture, for example, concentration-dependent uptake of a resource. Generally, $\boldsymbol{r}$ will also be impacted by flows of intermediates into or out of the system, denoted by $\boldsymbol{\sigma}$. We can then write the rate of change of the chemical environment as:

$$\frac{d\boldsymbol{r}}{dt} = \sum_\beta s_\beta \boldsymbol{f}_\beta(\boldsymbol{r}) + \boldsymbol{\sigma} \tag{1}$$

where s_β is the instantaneous abundance of species β. Importantly, this equation implies that the environment changes as a function of time t.

Secondly, the *sensitivity function* g_α describes the per-capita growth rate of a species α in a particular environment:

$$\frac{1}{s_\alpha}\frac{ds_\alpha}{dt} = g_\alpha(\boldsymbol{r}). \tag{2}$$

As defined here, these functions are very general, allowing expression of various relationships

between intermediates such as the extent to which different nutrients can be substituted for each other.[21]

Because g_α is dependent on $\boldsymbol{r}$, it is apparent that changes to the chemical environment caused by both α itself ($\beta = \alpha$, intra-specific interactions) and the other species ($\beta \neq \alpha$, inter-specific interactions) (Eq. 1) will regulate α's growth rate. Breaking this regulation into the effect mediated by each intermediate r_ρ individually, we can define 'elementary' metabolic interactions. These can be categorised into four classes by the combinations of the signs of the impact and sensitivity functions; following recently-defined terminology,[22,37] we refer to these here as enrichment (β produces a nutrient that enhances the growth of α), depletion (β reduces the concentration of a nutrient, impeding the growth of α), pollution (β produces a toxin that impedes the growth of α) and detoxification (β decreases the concentration of a toxin of α and enhances its growth) (Fig. 1A).

Species can interact via any combination of these elementary metabolic interactions, resulting in 'composite' metabolic interactions. In general, if all elementary interactions forming a composite interaction mediate a positive growth-rate effect on β (enrichment or detoxification) the measured interaction will also be positive, if all mediate a negative growth-rate effect (depletion or pollution) the measured interaction with be negative, and if they have a mixture of positive and negative impacts the sign of the measured interaction will depend on the environmental context (Fig. 1B).

We can capture this environmental dependency naturally within the impact/sensitivity function framework. In *closed* ecosystems (*i.e.* systems in which there are no external sources or sinks of intermediates, so $\boldsymbol{\sigma} = \mathbf{0}$), it can be shown (Supplementary Note 1) that

$$\frac{1}{s_\alpha}\frac{ds_\alpha}{dt} = g_\alpha(\boldsymbol{r}_0) + \sum_\beta \int_0^t a'_{\alpha\beta}(\boldsymbol{r})\; s_\beta \; d\tau, \tag{3}$$

where $\boldsymbol{r}_0$ is the initial environmental composition and the integral is taken over the entire history of the system up to the current time t (parameterised by τ). We will refer to this expression as the closed Environment-Organism (cEO) equation.

A key component of this expression is the *instantaneous interaction* $a'_{\alpha\beta}$, defined as

$$a'_{\alpha\beta}(\boldsymbol{r}) = \nabla g_\alpha(\boldsymbol{r}) \cdot \boldsymbol{f}_\beta(\boldsymbol{r}). \tag{4}$$

$\nabla g_\alpha(\boldsymbol{r})$ is the gradient of the sensitivity function, a vector field which denotes the direction in the environment space along which the growth rate of α increases most rapidly. The scalar product of this with $\boldsymbol{f}_\beta(\boldsymbol{r})$ (also a vector field) can therefore be naturally interpreted as indicating whether β is pulling the environment in a direction that increases (positive $a'_{\alpha\beta}$) or decreases (negative $a'_{\alpha\beta}$) the growth of α at a given position in the environment space $\boldsymbol{r}$. Put simply, this term captures the environmental dependency of the interaction in a given environment.

What do the other parts of this expression tell us about the dynamics of closed ecosystems? To answer this, it is instructive to compare the cEO equation with the familiar gLV equation:

$$\frac{1}{s_\alpha}\frac{ds_\alpha}{dt} = \mu_\alpha + \sum_\beta a_{\alpha\beta}\ s_\beta. \tag{5}$$

Here, μ_α is α's intrinsic growth rate (*i.e.* its growth in the absence of other species and at low population sizes) and $a_{\alpha\beta}$ is the interaction between β and α, defined as the population-dependent impact of β on the growth rate of α. We note some similarities between the two equations: both are expressed in terms of a basal growth rate added to a sum of interaction terms from all species β interacting with α. However, there are two important distinctions between the notion of interactions in the cEO and gLV frameworks. Firstly, as previously noted, $a'_{\alpha\beta}(\boldsymbol{r})$ is dependent on the environmental context. Moreover, this environment-dependence is not static - in general, closed ecosystems trace out some trajectory $\boldsymbol{r}(t)$ in the environment space, over which $a'_{\alpha\beta}(\boldsymbol{r})$ can vary dramatically. Indeed, we will soon see that in many systems it can change sign over time and space. Secondly, interactions in the EO framework are cumulative, arising from the integration of the interaction term over the entire history of the system. This reflects the fact that interactions are mediated via concentration changes in pools of different intermediates, which take time to be impacted by organisms. We refer to the resulting net impact of β on α's growth rate at a given time t ($\int_0^t a'_{\alpha\beta}(\boldsymbol{r})\ s_\beta\ d\tau$) as the *cumulative interaction*.

In the remainder of this manuscript, we discuss the consequences of the cEO equation for our understanding of the dynamics of closed ecosystems. Specifically, we show how the environ-

mental dependency of the instantaneous interaction results in temporal interaction dependencies and spatial structure when the environmental context changes over time and space (Fig. 1C).

2.2 Composite interactions can result in time-dependencies of interaction measurements

To develop and illustrate these ideas, we consider here one of the simplest composite interactions, a single species $\mathcal{A}$ interacting negatively with itself via nutrient depletion and positively via detoxification (Fig. 2A) in a well-mixed batch culture. We take the impact (Fig. 2B) and sensitivity functions (Fig. 2C) for this system from a previously described EO framework[11] (Methods). Calculation of the instantaneous intra-specific interaction $a'_{\mathcal{A}\mathcal{A}}$ (Fig. 2D) recapitulates the environmental dependency of interactions in this system, with positive intra-specific interactions generally dominating at high toxin concentrations and negative intra-specific interactions dominating at low toxin concentrations. This static map is traversed by the system as it evolves from some initial state $\boldsymbol{r}_0$, following the trajectory $\boldsymbol{r}(t)$. We can see in Fig. 2E that in this particular case, the system generally moves towards the origin as $\mathcal{A}$ reduces the concentration of both the nutrient $[n]$ and the toxin $[q]$. Importantly, this means that $a'_{\mathcal{A}\mathcal{A}}$ can switch from being positive early to being negative later on.

This switch in sign of the instantaneous intra-specific interaction propagates through to $\mathcal{A}$'s growth rate. As there are no other species in this system, the sole growth rate effect is the time-dependent impact of $\mathcal{A}$ on its own growth – the cumulative intra-specific interaction – given by $\int_0^t a'_{\mathcal{A}\mathcal{A}}(\boldsymbol{r})\ s_{\mathcal{A}}\ d\tau$. This switches from positive to negative once the accumulated benefit of the removal of the toxin is outweighed by the accumulated penalty from the reduction in the nutrient concentration (Fig. 2F). We now introduce a third quantity, the *measured interaction*, which is based on the abundance timecourses resulting from the integral of $\mathcal{A}$'s growth rate. This is an experimentally tractable value, closely related to the interaction measurements typically taken from batch-culture experiments[13] (see next section). In the simulated system, the sign switch in the instantaneous and cumulative interactions is reflected in a sign switch in this measured interaction (Fig. S1). We therefore arrive at an unexpected prediction: measurements of the intra-specific interaction in such systems should give positive values if performed early on (when detoxification dominates) and negative values if performed later (when depletion

dominates).

2.3 An antibiotic-based experimental system demonstrates sign-switching of the intra-specific interaction

We now attempted to establish whether this prediction was borne out in an experimental setting. As an experimental model of the detoxification/depletion interaction network (Fig. 2A), we made use of a bacterium (*Comamonas testosteroni*) that can degrade β-lactam antibiotics via induced secretion of β-lactamases (Fig. S2) and which can utilise proline as a sole carbon source. β-lactamase-producing bacteria are typically associated with a phenomenon known as the inoculum effect, in which larger starting population sizes result in higher measured Minimum Inhibitory Concentrations (MICs) of the antibiotic.[38,39] This is due to more rapid degradation of the antibiotic at larger initial population sizes, an effect already suggestive of a positive intra-specific interaction. Combined with a depletion mechanism mediated by competition over limited proline as a sole carbon source, we speculated that we would observe a positive to negative intra-specific interaction shift in a time-dependent manner as predicted theoretically.

To address this, we prepared arrays of environmental conditions (with varying initial proline, $[\text{pro}]_0$, and ampicillin, $[\text{amp}]_0$, concentrations) within 96-well plates (Fig. 3A). Each condition was split into two sets of wells, one inoculated with exponential-phase *C. testosteroni* cells at high density and the second at low density. Absorbance-based growth curves of these cultures were then measured in a plate reader.

In typical experimental measurements of interactions, monoculture and co-culture assays are prepared with a constant inoculation density of a focal species. The interaction is then measured by detecting whether this initial population grows more or less in the presence of a second species.[11,13,40,41] By direct analogy, we can treat our low inoculation density condition as a 'monoculture-like' assay, with a corresponding sub-population in the high-density condition which is of equal size. In the high-density condition, this sub-population is effectively co-cultured with a second sub-population of the same species. We can therefore measure the intra-specific interaction by comparing the fate of the matching sub-populations in the high- and low-density conditions (Fig. 3B).

In practice, this is achieved by dividing the growth curve of the high-density culture by the ratio of inoculation densities (4:1), yielding the size of the sub-population as a function of time.

At times when this normalised curve is higher than that of the low inoculation density condition, we can infer that the presence of additional cells of the same species enhanced the sub-population's growth - *i.e.* that a positive intra-specific interaction has occurred. The opposite argument applies when the normalised curve is lower than that of the low inoculation density condition (Fig. 3B). To measure the intra-specific interaction as a function of time, we can therefore simply subtract the low inoculation density curve from the normalised high inoculation density curve (Fig. 3C). We considered several alternative definitions of the measured interaction (Fig. S1D-G), but found that the chosen abundance difference metric provided the optimal balance between capturing the shape of the cumulative interaction and robustness to measurement noise. We note that it is similar to accepted endpoint-based interaction metrics,[13] although we emphasise that in contrast to these measurements which yield a single, fixed value, our approach yields a time-varying interaction estimate.

Beginning with the control conditions with zero antibiotic, we observe that the low inoculation density curves look very similar to the high inoculation density curves aside from a consistent time delay (Fig. S3A). We can interpret this delay as arising mostly from the smaller initial number of cells in the low density condition, as the ratio of densities between the two conditions remains approximately equal to the inoculation ratio until the high-density condition approaches stationary phase (at around 35 hrs). This is reflected in the abundance difference, which displays an approximately neutral intra-specific interaction up to this point and a negative interaction afterwards (Fig. 3D). In the presence of antibiotic the time delay between the two conditions increases, presumably because the smaller initial population takes longer to degrade the ampicillin before being able to start growing (Fig. S3B). Consequently, we see a concentration-dependent positive interaction emerging with increasing ampicillin doses, as predicted by the model (Fig. 3E). Ultimately however, all environments resulted in negative interactions in the long term. Summarising these experimental results by considering the peak and final abundance differences demonstrates the environmental and time dependencies together (Fig. 3F,G), which qualitatively match the patterns predicted by our modelling framework (Fig 3H,I). Although we do not directly fit model parameters to our data, we find that these qualitative patterns are robust to large changes in parameter values, suggesting that these results are not a result of fine-tuning of the model (Fig. S4).

Evolutionary rescue can result in similar abundance trajectories as those described here, as a

small number of mutant cells with antibiotic-resistant genotypes can grow to fixation after a long time delay.[42,43] We explored the role of evolution in our experimental system by measuring the MIC of ampicillin for each culture at the end of one of our interaction measurement timecourses (Fig. S5), finding that there was indeed a small increase ($\approx 50\%$) in the resistance of populations exposed to the highest ampicillin concentrations compared to those grown under antibiotic-free conditions. However, simulations incorporating the evolution of resistance showed that such events, far from driving the observed interaction time dependencies, tend to attenuate measured positive interactions if they have any effect at all (Fig. S6). Thus, we concluded that the consistent positive to negative interaction switch that we observe arises from the changing dominance of the two elementary interactions (detoxification and depletion), as suggested by our theoretical framework.

2.4 Small crossfeeding communities illustrate the common origins of time-dependent interactions and spatial structure

Thus far, we have considered time and environmental dependencies in a mono-species system. However, our framework generalises quite readily to multi-species communities, as well as certain types of spatially-structured communities (Methods, Supplementary Note 2, Fig. S7). Two recent studies have described time[33] and spatial[35] dependencies of very similar two-species communities. In both cases, a degrader species consumes a polymer (chitin or dextran) and subsequently produces a metabolite (acetate or glucose) which can be consumed by the second crossfeeding community member. When the polymer is exhausted, the degrader species can switch from net production to net consumption of the crossfed metabolite (Fig. 4A). Daniels et al.[33] note a time-dependency of the inter-specific interactions in batch culture: supply of an initial quantity of polymer leads initially to a strongly positive degrader $\rightarrow$ crossfeeder interaction and a neutral crossfeeder $\rightarrow$ degrader interaction, changing later to a weakly positive crossfeeder $\rightarrow$ degrader interaction and a weakly negative crossfeeder $\rightarrow$ degrader interaction (Fig. 4B). In a separate study, Wong et al.[35] loaded a similar community into a microfluidic device consisting of a single channel along which flow was applied. They observe that this community spontaneously self-structures along the channel, with the crossfeeding species only being able to grow towards its outlet (Fig. 4C). Given the commonalities between the two studies, we decided to use them as case studies for how our framework can unify similar observations occurring across time or space.

We built an EO model of the degrader/crossfeeder community, labelling the degrader population $\mathcal{D}$ and the crossfeeder population $\mathcal{C}$. We then derived expressions for the four different instantaneous interactions $a'_{\mathcal{DD}}$, $a'_{\mathcal{DC}}$, $a'_{\mathcal{CD}}$ and $a'_{\mathcal{CC}}$ (Methods). As shown in Fig. 4D, these four quantities can be arranged analogously to the interaction matrix of the gLV framework, with intra-specific interactions located along the main diagonal and inter-specific interactions located off this axis. However, instead of being represented by a single value as in the gLV approach, the instantaneous interactions are expanded into scalar fields defined on the entire environment space, capturing the environmental-dependency of each different interaction. Both the degrader's intra-specific instantaneous interaction $a'_{\mathcal{DD}}$ and inter-specific instantaneous interaction $a'_{\mathcal{CD}}$ contain both positive and negative regions, reflecting the changing balance between the enrichment mechanism (production of the crossfed metabolite from the polymer) and the depletion mechanism (competition over the crossfed metabolite) in different environments.

In batch culture, organisms modify their environment by secreting and consuming intermediates over time. A similar effect occurs in flowing systems, whereby the intermediates within a parcel of fluid are sequentially modified by the organisms residing at successive spatial locations as it is transported downstream. We can therefore project trajectories representing the evolution of the environment over time in a batch culture system (Fig. 4D, dashed lines) and the spatial variation of the environment along the length of a system under flow at steady-state (Fig. 4D, solid lines) onto these instantaneous interaction maps, allowing us to interpret the changing interactions over time and space using the same framework (Methods, Supplementary Note 2). The initial position of the system $\boldsymbol{r}_0$ – here assumed to consist of a large amount of polymer and zero crossfed metabolite – is interpreted subtly differently between the two cases: in batch culture, this represents the initial composition of the inoculum media, while in the microfluidic channel this represents the fixed composition of the media in the inflow of the device. Both systems sweep out initial trajectories with similar shapes, suggesting that the temporal patterning of the batch culture and the spatial patterning of the channel may arise from similar changes in interaction strengths.

To explore this in more detail, we now broke down the growth dynamics in the batch culture simulations into cumulative interactions, focusing on the inter-specific cases (Fig. 4E,F). We observe a similar pattern of the time evolution in the batch culture interactions as in the original study (Fig. 4B,E). In the initial phase, the large amount of initial polymer is metabolised by the

degrader, resulting in large amounts of overspill in the form of the crossfed metabolite. This consequently substantially enhances the growth of the crossfeeder, while the relatively low utility of the crossfed metabolite at this point for the degrader limits the impact of its uptake by the crossfeeder on the growth of the degrader. Later, the switch of the degrader to metabolite uptake leads to a decrease in the strength of the net-positive interaction with the crossfeeder, and a negative impact of the crossfeeder on the growth of degrader.

Very similar effects arise as we consider the spatially structured system (Fig. 4G,H). Near the inlet, the crossfeeder cannot grow as the rate at which it is washed out of the device (θ) exceeds the growth rate sustained at very low metabolite concentrations. However, the activity of the degrader leads to a gradual enhancement of the environment for the crossfeeder along the length of the channel and ultimately leads to the opening of a new niche when the cumulative interaction from the degrader to the crossfeeder exceeds the threshold set by θ. This leads to the spatial structure observed in the original study, with the crossfeeder only growing towards the outlet of the device (Fig. 4C,H). Our model also reproduces the suppressive effect of increased flow rates on the growth of the crossfeeder, as observed experimentally:[35] higher flowrates cause the environmental trajectory to terminate with less monomer and polymer having been consumed due to more rapid wash-out of the two substrates (Fig. S8A). Combined with a higher mortality θ associated with the stronger flow, this ultimately prevents the crossfeeder's niche from being efficiently opened up and halts its growth (Fig. S8B-G). In summary, our framework shows how spatial patterns arising under uni-directional flow and interaction time-dependencies in well-mixed systems are reflections of the same underlying ecological processes.

3 Discussion

Context dependencies have long been understood to be an important factor in ecological systems.[1,26,44–46] However, theoretical models that have attempted to capture these dependencies have generally done so via *ad hoc* manipulations of the interaction parameters,[47,48] rather than showing how these changes arise spontaneously out of the underlying reciprocal effects between organisms and their environment. By contrast, our approach shows how such dependencies emerge within EO models, which explicitly describe the bidirectional impact between the environment and the species within it. It also provides a theoretical framework to predict

interaction changes, given a hypothesis about the underlying metabolic processes at play in the ecosystem. We note that the long history of the EO framework[20–22,36,49] and its widespread use in microbial ecology[11,15,23,29,31,50,51] provides a wealth of existing experimental and theoretical results that may be re-interpreted through the cEO equation we derive in this study (Eq. 3).

Our results have particular relevance for our understanding of the outcomes of batch culture interaction measurements.[10–13,40,41] The mechanism by which measured interactions in batch culture switch from positive to negative over time once a single nutrient become limiting (Fig. 3) is quite general, and suggests that measurements based on end-point abundances may miss positive interactions during early community establishment. This may at least partially explain the ongoing controversy surrounding the relative distribution of negative and positive interactions in natural communities, where the predominance of negative interactions as estimated by end-point batch culture methods appears to be at odds with findings based on alternative approaches.[8,13,41,52,53]

We also note that despite our focus on microbial ecosystems, our results should also hold true for macroscopic ecosystems as long as the assumptions of our framework – particularly the assumption that the system is closed – are at least approximately true. Indeed, the role of the interplay between organisms and their environment has long been understood to drive successional dynamics in plant ecosystems, in which modification of the local environment by early pioneer species leads to the opening of new niches and eventual replacement of pioneers by latecomers better adapted for the new environment.[54] Similar successional patterns are observed in macroscopic systems such as whale falls[55] and microscopic systems such as marine snow.[18,56] In the language of our framework, successional effects would be represented as an accumulating, time-dependent positive interaction from pioneer species to latecomers. There may also be accumulating negative interactions from the latecomers to the pioneers, reflecting the tendency of pioneers to eventually be replaced during the successional sequence.[18] Likewise, although we have focused on microfluidic channels as models of systems under unidirectional flow, analogous systems such as rivers and the gut are widespread. The spatial niche-opening effects that our framework describes may therefore at least partially explain the longitudinal patterning of organisms in such systems.[57–59]

Another point of interest that this work sheds light on is the long-standing issue of higher order

interactions (HOIs) in microbial ecosystems, a phenomenon whereby the interaction between two partners is modulated by the presence of additional community members.[60,61] While HOIs have long been understood as arising from environment-organism feedbacks,[49,62,63] their appearance in microbial ecosystems is currently poorly accounted for. Our framework provides a simple explanation for these effects in closed systems: additional community members deflect the environmental trajectory $\boldsymbol{r}(t)$ (or $\boldsymbol{r}(x)$) from the path taken in the two-species case, changing the timecourse (or spatial pattern) of the instantaneous interactions experienced by both species and thereby altering their cumulative interactions. We therefore expect HOIs to be widely observed whenever more than two community members interact with a single intermediate, echoing simulational[62] and experimental[25] findings. We note however that many forms of HOI, such as those arising from phenotypic changes induced by a third species,[64] are not readily incorporated into EO models and consequently must be investigated by other means.

Nevertheless, there are some limitations to our framework. Perhaps most important is its limitation to closed ecosystems, contrary to most microbial communities in nature which are typically subject to external influxes and effluxes of material. In our framework, this assumption is expressed by assuming that the source term $\boldsymbol{\sigma}$ is equal to zero, but more generally a non-zero value of this term might represent the flow of resources into a well-mixed community (for example in a chemostat[65]) or diffusive transport of intermediates between neighbouring locations in a spatial model.[51] While we can derive an expression equivalent to the cEO equation for such open systems (Supplementary Note 1), the additional integral involving $\boldsymbol{\sigma}$ complicates its interpretation; certainly the analogy to the familiar gLV framework is lost. However, open systems more closely match the modelling assumptions of the gLV framework,[15] meaning direct gLV-based descriptions may be an appropriate alternative. Indeed, around an equilibrium point in an open system the quantity $a'_{\alpha\beta}$ becomes equivalent to the community matrix of the gLV framework $a_{\alpha\beta}$,[22] providing a tantalising connection between the two approaches. In addition, our assumption that indirect interactions dominate in microbial ecosystems, while well-supported for many systems,[16] cannot account for direct interaction mechanisms such as predation[66] or contact-dependent systems.[67] These may be incorporated into Eq. 3 simply by adding the standard gLV description of density-dependent interactions ($\sum_\beta a_{\alpha\beta} s_\beta$), although this hybrid direct/indirect interaction description is again less simple to interpret than the base cEO equation. We intend to address these extensions in future work.

In summary, our work shows that much of the diversity of interaction context-dependencies can be explained by reciprocal feedbacks between organisms and their environment. We give multiple examples of how explicit theoretical representation of these feedbacks can be used to predict and interpret interaction changes, providing a path forwards in the effort to manipulate interactions to predictable ends. Ultimately, we anticipate that a renewed focus on the role of the environment in determining the properties of microbial ecosystems will open new methods for controlling communities, as well as help to resolve longstanding questions regarding their composition and diversity.

4 Acknowledgements

We would like to thank E. Ulrich, M. Amicone, S. Sulheim, C. Vulin, A. Del Panta, P.Padmanabha, G. Ugolini and J. Palmer for their valuable comments on a previous version of this manuscript. We would also like to thank J. Wong for sharing microfluidic data. OJM was supported by an HFSP long-term fellowship (LT0020/2022-L), while SM was supported by the NCCR Microbiomes and an Eccellenza grant both from the Swiss National Science Foundation.

5 Data and code availability statement

All data and code used in this study (apart from data reproduced from other studies, Fig. 4B,C) is available at https://github.com/Mitri-lab/enviroInteracts.

6 Materials and methods

6.1 Modelling

6.1.1 Toxin-nutrient model

Our single-species toxin-nutrient model (Fig. 2A) is adapted from a previously described EO framework.[11] We model the growth rate of a single species $\mathcal{A}$, with abundance denoted as $s_{\mathcal{A}}$, as being positively dependent upon the concentration of a nutrient $[n]$ and negatively dependent upon the concentration of a toxin $[q]$. We assume that both of these positive and negative growth impacts are saturating functions of their respective intermediates, modelled as Monod functions. We further assume that the concentrations of the intermediates are measured in units of the half-velocity constant of the two Monod terms and that a fraction f of the utilised nutrient is invested into detoxification and the remainder into growth. Together, these assumptions give the per-capita growth rate as

$$\frac{1}{s_{\mathcal{A}}}\frac{ds_{\mathcal{A}}}{dt} = (1-f)\frac{\nu_n[n]}{[n]+1} - \frac{\nu_q[q]}{[q]+1}, \tag{6}$$

where ν_n is the maximal nutrient uptake rate and ν_q is the maximal toxin impact.

The impact functions of the original model incorporate a yield parameter that describes the efficiency at which resources are converted into biomass.[11] However, we can remove this parameter by non-dimensionalisation if we define the bacterial abundance $s_{\mathcal{A}}$ as being measured in terms of the amount of biomass produced by one unit of nutrient with zero toxin degradation investment ($f = 0$) and zero toxin ($[q] = 0$). Then we can write the nutrient dynamics as

$$\frac{d[n]}{dt} = -s_{\mathcal{A}}\frac{\nu_n[n]}{[n]+1}. \tag{7}$$

Toxin dynamics are modelled similarly but involve an additional term, the detoxification efficiency δ, which sets the amount of toxin removed from the environment for each unit of nutrient invested. Thus we obtain

$$\frac{d[q]}{dt} = -s_{\mathcal{A}}\delta f[q]\frac{\nu_n[n]}{[n]+1}. \tag{8}$$

For simplicity, we do not incorporate a passive (nutrient-independent) toxin uptake term as in.[11]

Defining the environment vector $\boldsymbol{r} = \begin{pmatrix} [n] \\ [q] \end{pmatrix}$, the impact function $\boldsymbol{f}_{\mathcal{A}}(\boldsymbol{r})$ can be written from Eqs. 7 and 8 as

$$\boldsymbol{f}_{\mathcal{A}}(\boldsymbol{r}) = -\frac{\nu_n[n]}{[n]+1}\begin{pmatrix} 1 \\ \delta f[q] \end{pmatrix}. \tag{9}$$

We note that Eq. 6 is already in the form of a sensitivity function $g_{\mathcal{A}}(\boldsymbol{r})$. We can therefore derive its gradient as

$$\nabla g_{\mathcal{A}}(\boldsymbol{r}) = \begin{pmatrix} \frac{(1-f)\nu_n}{([n]+1)^2} \\ \frac{-\nu_q}{([q]+1)^2} \end{pmatrix}, \tag{10}$$

and so,

$$a'_{\mathcal{A}\mathcal{A}} = \nabla g_{\mathcal{A}}(\boldsymbol{r}) \cdot \boldsymbol{f}_{\mathcal{A}}(\boldsymbol{r}) = \frac{\nu_n[n]}{[n]+1}\left(\nu_q \delta f \frac{[q]}{([q]+1)^2} - (1-f)\frac{\nu_n}{([n]+1)^2}\right), \tag{11}$$

with a non-trivial nullcline $a'_{\mathcal{A}\mathcal{A}} = 0$ at

$$[n] = -1 + \sqrt{\frac{(1-f)\nu_n([q]+1)^2}{[q]f\delta\nu_q}}. \tag{12}$$

Parameter values for this model as used in this manuscript are given in table 1. These were not explicitly fitted to our experimental data but were chosen to qualitatively match our experimental results, representing a regime in which the toxin has a comparable negative growth rate impact as the nutrient's positive impact ($\nu_n = \nu_q$) but is efficiently degraded with a relatively low degradation investment. Given our non-dimensionalisation of the half-velocity constants, the range of initial concentrations $[n]_0$ and $[q]_0$ shown in Fig. 3H,I is also of significance; our choice of $0.5 < [n]_0 < 5$ and $[q]_0 < 0.5$ indicates that the nutrients are close to saturation for most of the simulated conditions, while the toxin will have an approximately linearly concentration-dependent effect. Large changes to these parameter values do not generally have a strong effect on the overall interaction patterns, although we do observe qualitatively different outcomes

ν_n	ν_q	f	δ
0.05	0.05	0.2	10

Table 1: Parameter values used for the toxin-nutrient model of section 6.1.1

when the strength of the toxin compared to the nutrient is increased to such an extent that it entirely abolishes growth in either the low inoculation density condition or both conditions (Fig. S4).

6.1.2 Degrader-crossfeeder model

We model the system described in Fig. 4A by considering the dynamics of the degrader population $\mathcal{D}$, the crossfeeder population $\mathcal{C}$, the polymer p and the crossfed metabolite m. We assume that $\mathcal{D}$ consumes p according to Monod kinetics, utilising a fixed fraction $1-\phi$ for its own growth and converting the remaining fraction ϕ into m. This is in turn utilised by both $\mathcal{C}$ and $\mathcal{D}$ for growth, again according to Monod kinetics.

We note that our model is structured such that $\mathcal{D}$ has priority access to the breakdown products of p. In similar systems, these breakdown products act as extracellular public goods, with both degraders and crossfeeders having equal access to them.[68] However, in the studies we consider here, two similar mechanisms preserve the priority status of the degrader: in Wong et al.[35], the degrader *Bacteroides thetaiotaomicron* appears to import dextran and degrade it internally, as suggested by the upregulation of various nutrient importers and cytosolic dextranases in the presence of dextran. The breakdown products - principally glucose - can therefore largely be maintained as internal private goods, with the excess leaking out and acting as the nutrient source for the crossfeeder *Bacteroides fragilis*. Similarly, while the degrader *Vibrio natriegens* of Daniels et al.[33] does appear to release digestive enzymes to break down chitin externally, the resulting breakdown products cannot be metabolised directly by the crossfeeder *Alteromonas macleodii*. Instead, they must first be converted to acetate by the internal catabolic metabolism of the degrader. Thus, the crossfeeder must again wait until the substrate has passed through a stage in which it is a private good of the degrader, effectively separating the two species into different trophic levels.[69]

Denoting the environment vector $\boldsymbol{r} = \begin{pmatrix} [p] \\ [m] \end{pmatrix}$ and subscripting yield parameters Y, half-saturation constants K and maximal rate constants ν with labels denoting species and intermediate, this model is described by the sensitivity functions

$$g_{\mathcal{D}}(\boldsymbol{r}) = (1-\phi)\frac{\nu_{\mathcal{D}p}[p]}{[p]+1} + \frac{\nu_{\mathcal{D}m}[m]}{[m]+K_{\mathcal{D}m}}, \tag{13a}$$

$$g_{\mathcal{C}}(\boldsymbol{r}) = \frac{\nu_{\mathcal{C}m}[m]}{[m]+K_{\mathcal{C}m}}. \tag{13b}$$

Note that a similar non-dimensionalisation has been applied here as for the toxin-nutrient model, with the polymer concentration being measured in terms of the half-saturation constant for the degrader ($K_{\mathcal{D}p}$).

We also have corresponding impact functions given by:

$$\boldsymbol{f}_{\mathcal{D}}(\boldsymbol{r}) = \begin{pmatrix} -\frac{\nu_{\mathcal{D}p}[p]}{[p]+1} \\ \phi\frac{\nu_{\mathcal{D}p}[p]}{[p]+1} - \frac{1}{Y_{\mathcal{D}m}}\frac{\nu_{\mathcal{D}m}[m]}{[m]+K_{\mathcal{D}m}} \end{pmatrix}, \tag{14a}$$

$$\boldsymbol{f}_{\mathcal{C}}(\boldsymbol{r}) = \begin{pmatrix} 0 \\ -\frac{1}{Y_{\mathcal{C}m}}\frac{\nu_{\mathcal{C}m}[m]}{[m]+K_{\mathcal{C}m}} \end{pmatrix}, \tag{14b}$$

where the yield constant $Y_{\mathcal{D}p}$ has likewise been eliminated via non-dimensionalisation, along with a factor specifying the number of units of metabolite produced per unit of polymer.

The gradients of the sensitivity functions are given as

$$\nabla g_{\mathcal{D}}(\boldsymbol{r}) = \begin{pmatrix} (1-\phi)\frac{\nu_{\mathcal{D}p}}{([p]+1)^2} \\ \frac{\nu_{\mathcal{D}m}K_{\mathcal{D}m}}{([m]+K_{\mathcal{D}m})^2} \end{pmatrix}, \tag{15a}$$

$$\nabla g_{\mathcal{C}}(\boldsymbol{r}) = \begin{pmatrix} 0 \\ \frac{\nu_{\mathcal{C}m}K_{\mathcal{C}m}}{([m]+K_{\mathcal{C}m})^2} \end{pmatrix}, \tag{15b}$$

leading to the instantaneous interactions

$\nu_{\mathcal{D}p}$	$\nu_{\mathcal{D}m}$	$\nu_{\mathcal{C}m}$	$Y_{\mathcal{D}m}$	$Y_{\mathcal{C}m}$	$K_{\mathcal{D}m}$	$K_{\mathcal{C}m}$	ϕ
1	1	1	1	1	1	1	0.6

Table 2: Parameter values used for the degrader-crossfeeder model of section 6.1.2

$$a'_{\mathcal{C}\mathcal{C}}(\boldsymbol{r}) = -\frac{1}{Y_{\mathcal{C}m}}\frac{\nu^2_{\mathcal{C}m}K_{\mathcal{C}m}[m]}{([m]+K_{\mathcal{C}m})^3}, \tag{16a}$$

$$a'_{\mathcal{C}\mathcal{D}}(\boldsymbol{r}) = \frac{\nu_{\mathcal{C}m}K_{\mathcal{C}m}}{([m]+K_{\mathcal{C}m})^2}\left(\phi\frac{\nu_{\mathcal{D}p}[p]}{[p]+1} - \frac{1}{Y_{\mathcal{D}m}}\frac{\nu_{\mathcal{D}m}[m]}{[m]+K_{\mathcal{D}m}}\right), \tag{16b}$$

$$a'_{\mathcal{D}\mathcal{C}}(\boldsymbol{r}) = -\frac{1}{Y_{\mathcal{C}m}}\frac{\nu_{\mathcal{D}m}K_{\mathcal{D}m}}{([m]+K_{\mathcal{D}m})^2}\frac{\nu_{\mathcal{C}m}[m]}{([m]+K_{\mathcal{C}m})}, \tag{16c}$$

$$a'_{\mathcal{D}\mathcal{D}}(\boldsymbol{r}) = (\phi-1)\frac{\nu^2_{\mathcal{D}p}[p]}{([p]+1)^3} + \frac{\nu_{\mathcal{D}m}K_{\mathcal{D}m}}{([m]+K_{\mathcal{D}m})^2}\left(\phi\frac{\nu_{\mathcal{D}p}[p]}{[p]+1} - \frac{1}{Y_{\mathcal{D}m}}\frac{\nu_{\mathcal{D}m}[m]}{[m]+K_{\mathcal{D}m}}\right). \tag{16d}$$

The non-trivial nullcline of the inter-specific instantaneous interaction $a'_{\mathcal{C}\mathcal{D}} = 0$ is given by

$$[p] = \frac{[m]\nu_{\mathcal{D}m}}{\phi\nu_{\mathcal{D}p}Y_{\mathcal{D}m}([m]+K_{\mathcal{D}m}) - \nu_{\mathcal{D}m}[m]}. \tag{17}$$

The nullcline of the intra-specific instantaneous interaction $a'_{\mathcal{D}\mathcal{D}} = 0$ was found numerically using scipy's root function.

Parameter values for this model are given in table 2. Similarly to the toxin-nutrient model these are not explicitly fitted to the experimental data, and indeed we expect that they are substantially different between the two systems used in the studies we discuss here.[33,35] Such a qualitative approach does, however, allow us to determine the minimal differences between the underlying metabolic processes needed to bring about the observed interaction patterns in both systems. In particular, we find that we can reproduce the observed patterns if all metabolic processes (polymer degradation by the degrader and monomer uptake by both species) have equivalent kinetics ($\nu_{\mathcal{D}p} = \nu_{\mathcal{D}m} = \nu_{\mathcal{C}m}$ and $K_{\mathcal{D}m} = K_{\mathcal{C}m}$), the yields of the monomer and polymer are equal ($Y_{\mathcal{D}m} = Y_{\mathcal{C}m}$) and a fairly high proportion of polymer is converted to monomer and secreted ($\phi = 0.6$). We also assume that the polymer is introduced at a concentration below the corresponding half-velocity constant of the degrader ($[p]_0$=0.8), meaning the rate of polymer degradation will be strongly impacted by concentration changes over time and/or space.

6.1.3 Batch culture simulations

To generate trajectories representing the time evolution of batch culture experiments, the coupled systems of ODEs for both models were numerically integrated using scipy's solve_ivp function, using the Runge-Kutta method of order 5(4). The starting population sizes for the toxin-nutrient model were 0.001 (low inocultion density) and 0.004 (high inoculation density), while both the degrader and crossfeeder populations were initiated at a density of 0.01 for the degrader-crossfeeder model. Initial environmental compositions ($\boldsymbol{r}_0$) are indicated in the relevant figures.

6.1.4 Microfluidic simulations

Our simulations of spatially-structured flowing systems require that we move from a purely temporal model of intermediate and species changes to a spatio-temporal model. To do this, we represent the concentration profiles of the full set of intermediates as a set of 1D scalar fields $\boldsymbol{r}(x,t)$, with the position along the channel represented by the spatial coordinate x. This varies from the inlet position $x = 0$ to the outlet position $x = L$. Likewise, the profile of the species abundances $\boldsymbol{s}$ is represented by the set of 1D scalar fields $\boldsymbol{s}(x,t)$. Implicitly, we assume that the system is small enough in the y and z dimensions that it is effectively well-mixed along these axes by diffusion, allowing us to make use of the 1D approximation to study longitudinal structure.

We simulate the dynamics of the media composition using the 1D advection-diffusion equation:

$$\frac{\partial \boldsymbol{r}(x,t)}{\partial t} = D\frac{\partial^2 \boldsymbol{r}(x,t)}{\partial x^2} - v_x\frac{\partial \boldsymbol{r}(x,t)}{\partial x} + R. \tag{18}$$

Here, on the right hand side, the first term represents the diffusive fluxes of intermediates along the length of the channel, with a rate set by the diffusion coefficient $D = 0.5$ which we take to be equal for all intermediates. This value is high enough to ensure numerical stability of the resulting environmental trajectories. The second term represents the advective fluxes mediated by active flow, with a rate set by the flow velocity v_x. We choose values of v_x to ensure that advection dominates over diffusion given the channel length L and the diffusion coefficient D, a necessary condition of our framework (Supplementary Note 2). The final term represents

the sources and sinks of intermediates at each position, in this case given by an adjusted form of the impact functions for the degrader-crossfeeder model (Eq. 14). Together, these terms give the total rate of change of the intermediate concentrations at a particular location in the channel. Microbial population dynamics are simulated at each spatial location and are assumed to grow statically (*i.e.* to not be transported by diffusion or flow), with local dynamics based on an adjusted form of the sensitivity functions of the degrader-crossfeeder model based on the local concentrations of intermediates (Eq. 13). We describe the necessary adjustments to the impact and sensitivity functions next, along with their implications for the calculation of the cumulative interaction.

As we discuss in Supplementary Note 2, application of our framework to such systems requires that the dynamics approach a steady-state. To ensure this, we make two additions to our impact and sensitivity functions. Firstly, we assume that the microbial populations can grow only to a maximal density at a given location along the device, given by the channel capacity $\lambda = 1$. This is applied to each population independently in order to prevent a inter-specific density dependence, which would act as a direct interaction which could not be integrated into our framework; the maximal *total* abundance at a given site is therefore equal to λ multiplied by the number of different populations. Both growth rates and associated impacts on concentrations of intermediates slow down as this capacity is approached. Secondly, we assume that microbes are flushed out of the system by flow at a rate $\theta = 0.005\ v_x$, analogous to the wash-out term in chemostat models.[65] The dependence of this wash-out rate on the flow rate v_x is based on observations that suggest that biofilms are more strongly eroded at higher flow rates.[35,70] Microbial growth rates are therefore given as

$$\frac{1}{s_\alpha(x,t)}\frac{ds_\alpha(x,t)}{dt} = \frac{\lambda - s_\alpha(x,t)}{\lambda} g_\alpha(\boldsymbol{r}(x,t)) - \theta, \tag{19}$$

while the effective impact rates on the intermediates are given as

$$\frac{d\boldsymbol{r}(x,t)}{dt} = \sum_\beta \boldsymbol{f}_\beta(\boldsymbol{r}(x,t)) s_\beta(x,t) \frac{\lambda - s_\beta(x,t)}{\lambda}. \tag{20}$$

This latter expression is the explicit form of the term R in Eq. 18.

The introduction of this density-dependent scaling term in the dynamics of the intermediates

also requires an adjustment in the way the cumulative interaction is calculated. This arises because this term slows down the simulated metabolic rate of cells at high densities, reducing their effective impact on their environment. Once steady-state is achieved (Supplementary Note 2), the microbial abundances and resource concentrations become dependent solely on the position in the channel ($\boldsymbol{r}(x,t) \to \boldsymbol{r}^*(x)$ and $\boldsymbol{s}(x,t) \to \boldsymbol{s}^*(x)$). The cumulative interaction from β to α is therefore given as $\frac{1}{v_x}\int_0^x a'_{\alpha\beta}(\boldsymbol{r}^*)s^*_\beta \frac{\lambda - s^*_\beta}{\lambda} d\chi$. Here, χ acts as a variable that parameterises the spatial trajectory of the system from the inlet to the query position x, analogously to how τ parameterises the temporal trajectory of batch-culture systems in Eq. 3.

To ensure the simulated composition of the inflowing media remains fixed, we set $\frac{d\boldsymbol{r}(x=0,t)}{dt} = 0$. Additionally, we use an absorbing boundary condition at $x = L$ to simulate free variation of the composition of the media at the outlet. The initial composition of the environment was set uniformly as $\boldsymbol{r}(x, t = 0) = \boldsymbol{r}_0$, *i.e.* equal to the composition of the inflow.

Both populations were seeded uniformly throughout the system at a density of $\boldsymbol{s}(x, t = 0) = 0.01$. The set of PDEs was numerically integrated using the solve_ivp function. We simulated dynamics for $t = 1000$ time units until the system reached a steady-state (Fig. S7), allowing application of our theoretical framework.

M9 10x	K_2HPO_4	30 g
	NaCl	5 g
	NH_4Cl	10 g
	Na_2HPO_4	60 g
Metals 44 1000x	$Na_2EDTA \cdot 2H_2O$	0.387 g
	$ZnSO_4 \cdot 7H_2O$	1.095 g
	$FeSO_4 \cdot 7H_2O$	0.914 g
	$MnSO_4 \cdot 7H_2O$	0.154 g
	$CuSO_4 \cdot H_2O$	0.0392 g
	$Co(NO_3)_2 \cdot 6H_2O$	0.0284 g
	$Na_2B_4O_7 \cdot 10H_2O$	0.0177g
	H_2O	to 1 l
Hutner's mineral base (HMB) 50x	Nitric triacetic acid (NTA)	10 g
	$MgSO_4 \cdot 7H_2O$	14.45 g
	$CaCl_2 \cdot 2H_2O$	3.33 g
	$(NH_4)_6Mo_7O_24 \cdot 4H_2O$	0.00974 g
	$FeSO_4 \cdot 7H_2O$	0.099 g
	Metals 44 1000x	50 ml
	H_2O	to 1 l
Base minimal media	HMB 50x	20 ml
	M9 10x	100 ml
	H_20	850 ml

Table 3: Composition of base minimal media.

6.2 Experiments

6.2.1 Strains and growth conditions

Our *C. testosteroni* strain MWF001 comes from a pre-existing study.[11] Cells were streaked onto TSA plates from freezer stocks and grown overnight. Single colonies were then picked (one colony per biological replicate), and cells grown overnight in glass Erlenmeyer flasks under continuous shaking in base minimal media (Table 3) supplemented with 10 mM proline. Due to the slow growth of *C. testosteroni* under these conditions, cells were in exponential phase at the end of this period. Cells were then washed twice in PBS. The OD_{600}s of the washed cultures were then measured and cultures diluted to initialise experiments at the appropriate starting densities as described below. Cultures were grown at 28°C in all cases.

6.2.2 β-lactamase activity measurements

Exponential-phase cultures of *C. testosteroni* were inoculated into two Erlenmeyer flasks containing 20 ml of minimal media supplemented with 5mM proline at a starting OD_{600} adjusted to 0.00025. To one of these flasks we added ampicillin at a label concentration of 100 μg ml^{-1},

however subsequent experiments suggested that degradation of our antibiotic freezer stocks had reduced the effective concentration to $\approx$ 30 μg ml^{-1}. The resulting cultures were grown under continuous shaking, and samples taken at 0, 6, 30, 54 and 78 hr. To measure the extracellular β-lactamase activity of cultures, samples were first spun down and the supernatant pipetted off. The enzymatic activity of the supernatant was then measured using a β-lactamase activity assay kit (Sigma-Aldrich, MAK221). In Fig. S2, the β-lactamase detection limit is defined as two times the standard deviation of the signal estimated from sample-free control wells.

6.2.3 Intra-specific interaction measurements

We prepared 96-well plates with a variety of environmental conditions by filling each well with 180 μl of basal media supplemented with varying concentrations of proline ([pro]$_0$ = 0.5, 1, 2, 5 mM) and ampicillin ([amp]$_0$ = 0, 10, 20, 30 μg ml^{-1}). 20 μl of an exponential-phase culture of *C. testosteroni* was then added, with three wells of each condition containing culture adjusted to high density (OD$_{600}$ in well = 0.004) and three wells containing culture adjusted to low density (OD$_{600}$ in well = 0.001). The plate was placed into a plate reader (BioTek Synergy H1) and OD$_{600}$ readings for each well taken every 30 mins for 120 hr at 28 °C under continual shaking between timepoints. The background signal was subtracted from the resulting raw growth curves by first estimating the OD contribution from the cells in the high inoculation OD wells (κ) using the equation

$$\kappa = \frac{4}{3}(< \mathrm{OD}_h(0) > - < \mathrm{OD}_l(0) >), \tag{21}$$

where $< \mathrm{OD}_h(0) >$ and $< \mathrm{OD}_l(0) >$ represent the plate-wide average initial OD readings for the high inoculation density and low inoculation density wells, respectively. The factor of $\frac{4}{3}$ stems from the 1:4 inoculation density ratio. Each curve was now individually adjusted by subtracting the average OD of the specified curve's first 3 timepoints and adding either κ for the high inoculation density wells or $\frac{\kappa}{4}$ for the low inoculation density wells. The average OD curves were then calculated from the three replicates for each condition and used to calculate the abundance differences shown in Fig. 3D-G.

6.2.4 MIC measurements

To confirm that the intrinsic resistance of *C. testosteroni* had not changed over the duration of the intra-specific interaction assay, we measured the Minimum Inhibitory Concentration (MIC) of ampicillin for each of the cultures in the 96-well plate at the end of one biological replicate of our experiment. Concentration gradients of ampicillin were first prepared in 96-well plates containing LB media, to which we added samples from the interaction measurement plate (specifically, from the low inoculation density wells as these were subject to the strongest selective pressure). As the β-lactamase resistance mechanism results in different MICs based on the starting density of culture (the inoculum effect[38,39]), we adjusted the inoculation volume to ensure approximately equal numbers of cells were added regardless of the final density of the cultures being measured. To do this, we took advantage of the fact that the final density of the samples was directly proportional to the initial proline concentration $[\text{pro}]_0$ (Fig. S5A), allowing us to simply scale the inoculation volume by $[\text{pro}]_0$. Specifically, we used 20 μl of $[\text{pro}]_0$ = 0.5 mM cultures, 10 μl of $[\text{pro}]_0$ = 1 mM cultures, 5 μl of $[\text{pro}]_0$ = 2 mM cultures and 2 μl of $[\text{pro}]_0$ = 5 mM cultures. These inoculua resulted in starting densities around 10 times greater than those of the interaction assay, explaining why the resulting MICs were substantially higher than the values of $[\text{amp}]_0$ used during interaction measurements. The total volume in each well was fixed at 200 μl. Plates were incubated at 28°C under continuous shaking. Final MICs were defined as the lowest concentration of ampicillin at which the OD_{600} of a given sample was reduced by at least 80% relative to an antibiotic-free control after 20 hrs.

7 Figures

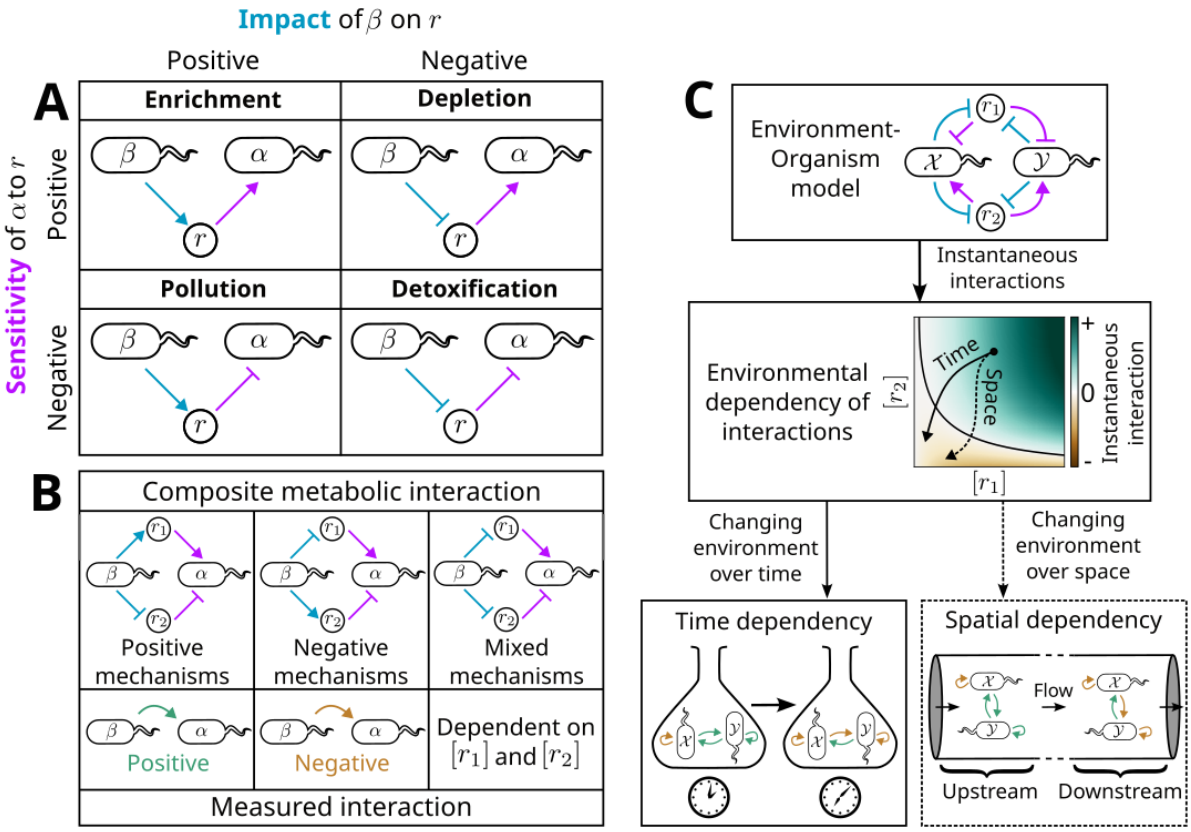

Figure 1: **Multiple interaction context-dependencies are explained with a single theoretical framework. A** Indirect interactions between organisms - those mediated by changes in the abundance of intermediates - can be broken into elementary components by considering the role of each intermediate r_ρ separately. The 'sensitivity function' of a target species α with respect to a given intermediate r (purple) denotes the effect of r on the growth rate of α (*i.e.* whether it is a toxin – bar – or nutrient – arrow), while the 'impact function' of an effector species β with respect to r (blue) denotes the effect of β on the abundance of r (*i.e.* whether it is produced – arrow – or consumed – bar). Combinations of the signs of these functions imply four elementary metabolic interaction types: enrichment and detoxification which enhance the growth of the impacted species α, and depletion and pollution which reduce α's growth.[22,37] **B** These can be combined to generate composite metabolic interactions, with the sign of the measured interaction depending on the individual effects of the composed elementary metabolic interactions. In cases where the elementary interactions have a mixture of positive and negative growth rate impacts, the measured interaction will depend on the relative concentrations of the intermediates - *i.e.* the environmental context. **C** Our theoretical framework shows how Environment-Organism (EO) models in which such indirect interaction mechanisms are explicitly represented give rise to an instantaneous interaction that depends on the environment. As the environment changes over time (*e.g.* in batch culture) or over space (*e.g.* in microfluidic channels at steady-state), this environmental dependency in turn gives rise to time and spatial dependencies.

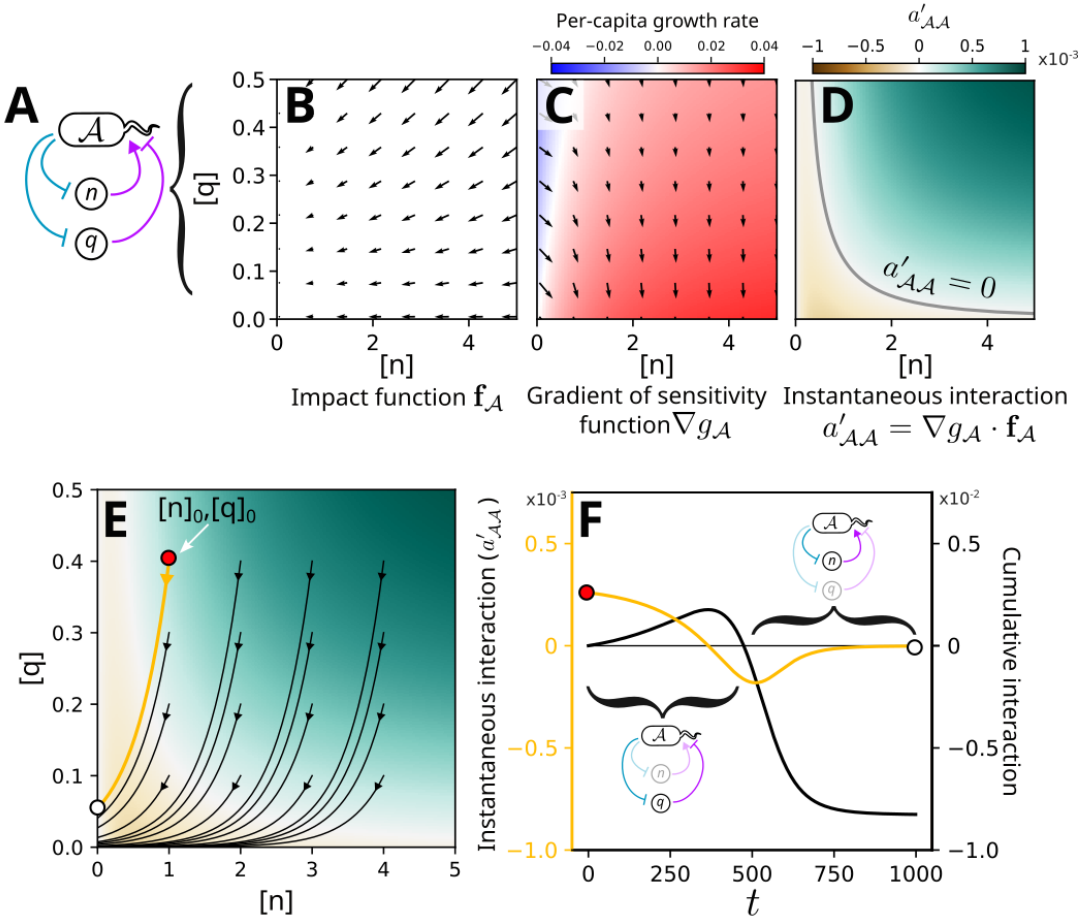

Figure 2: **Intra-specific interactions mediated by mixtures of positive and negative mechanisms are predicted to switch sign over time in batch culture.** **A** One of the simplest examples of a system with mixed pairwise elementary interactions is a single species $\mathcal{A}$ which increases the growth of other members of its population by detoxifying an environmental toxin while reducing their growth by depleting a common nutrient. **B**, **C** We can represent the impact and sensitivity functions for $\mathcal{A}$ using the 'environment space', which denotes the concentrations of the different intermediates in the system (in this case, the concentrations of the nutrient $[n]$ and of the toxin $[q]$). Impact functions are vector fields sitting in this space (black arrows, **B**), while sensitivity functions are scalar fields (**C**). The gradient of the sensitivity function then represents the direction in the environment space in which the growth rate of $\mathcal{A}$ increases most rapidly, as well as how quickly it increases (black arrows, **C**). **D** Taking the scalar product of the impact function and the gradient of the sensitivity function yields the instantaneous interaction $a'_{\mathcal{A}\mathcal{A}}$, representing the instantaneous effect that $\mathcal{A}$ has on its own growth rate at a given position in the environment space. **E** Closed systems such as batch culture experiments trace out trajectories in this environment space, starting from an initial position $[n]_0$, $[q]_0$. **F** We can calculate both $a'_{\mathcal{A}\mathcal{A}}$ and the integrated effect of $\mathcal{A}$ on its own growth (main text), demonstrating a switch in the effective intra-specific interaction: at early timepoints, when the toxin concentration is high, detoxification dominates and the interaction appears positive. By contrast, at late timepoints when the toxin has mostly been removed, depletion of the single nutrient dominates and the instantaneous intra-specific interaction becomes negative.

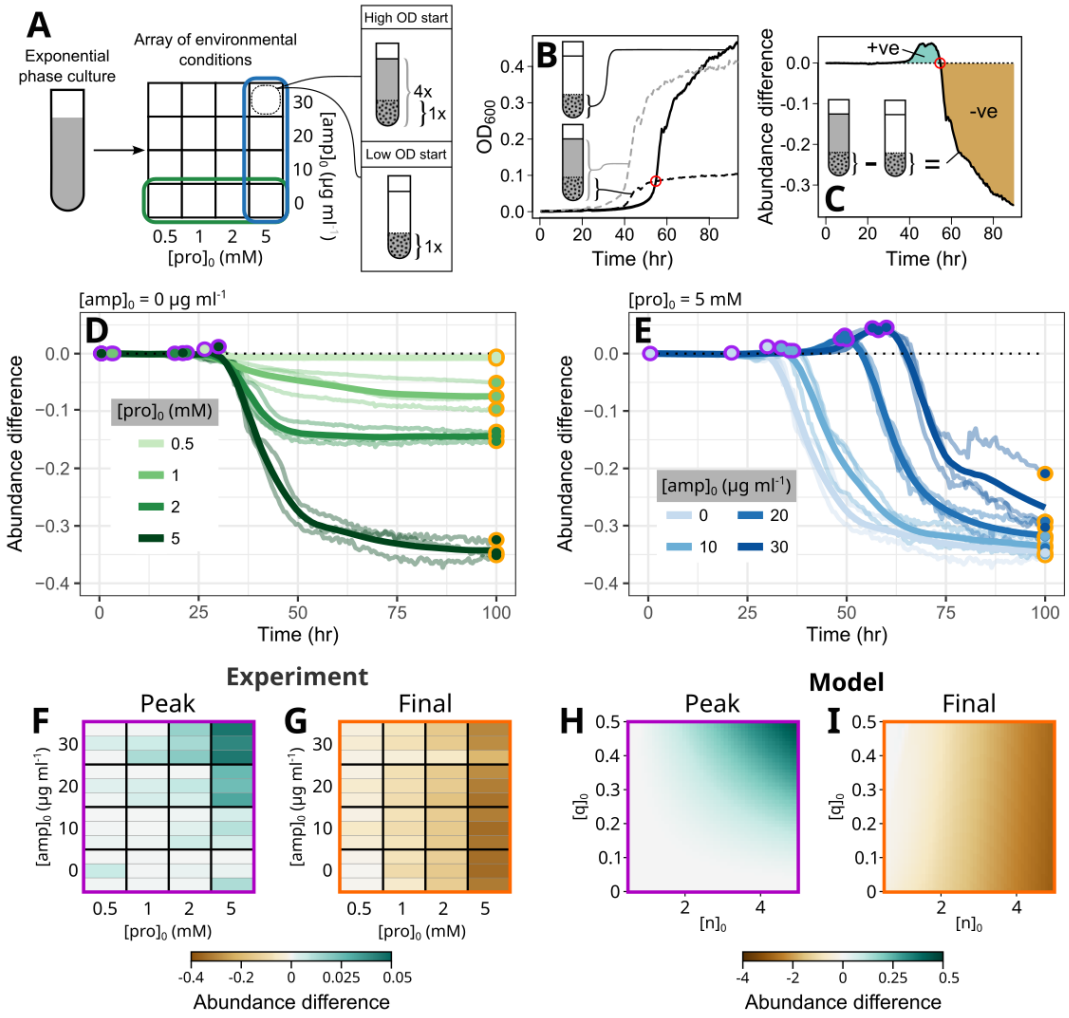

Figure 3: **An antibiotic-based model system demonstrates sign switching of measured intra-specific interactions over time.** *Comamonas testosteroni* is a β-lactamase producing soil bacterium which can degrade environmental ampicillin. Combined with competition over a single limiting carbon source (proline), we used this as an experimental analogue of the model shown in Fig. 2. **A** Exponential-phase cells were transferred to a 96-well plate containing wells with different initial ampicillin concentrations $[\text{amp}]_0$ and proline concentrations $[\text{pro}]_0$. Six wells were prepared for each condition, consisting of three replicates each of low and high initial inoculation densities at a 1:4 density ratio. **B**, **C** We measured the growth curve of each well and averaged the technical replicates. We then calculated the abundance difference over time by normalising the averaged high OD curve by the ratio of the starting ODs (**B**) and subtracting the low OD curve (main text, Fig. S1) (**C**). Abundance differences greater than 0 indicate that growth of a matched sub-population of *C. testosteroni* (black dots) was enhanced by the presence of additional members of the same species in the high-OD wells relative to the low-OD wells (a positive intra-specific interaction), while differences less than 0 indicate growth suppression (a negative intra-specific interaction). **D**, **E** Comparing abundance differences across different proline (**D**) and ampicillin (**E**) concentrations demonstrates the environment-dependent shift in positive to negative interactions predicted by the model. We summarise this shift for each condition by measuring the peak (purple circles) and final (orange circles) abundance difference for each condition (**F**,**G**). **H**,**I** These qualitatively match predictions from our modelling framework. The general pattern that emerges from these simulations is robust to changes in simulation parameters (Fig. S4). Faint lines in **D** indicate $n = 3$ separate biological replicates performed on separate days, while bold lines indicate LOESS-smoothed averages. Biological replicates are indicated in **F** and **G** by separate horizontal strips.

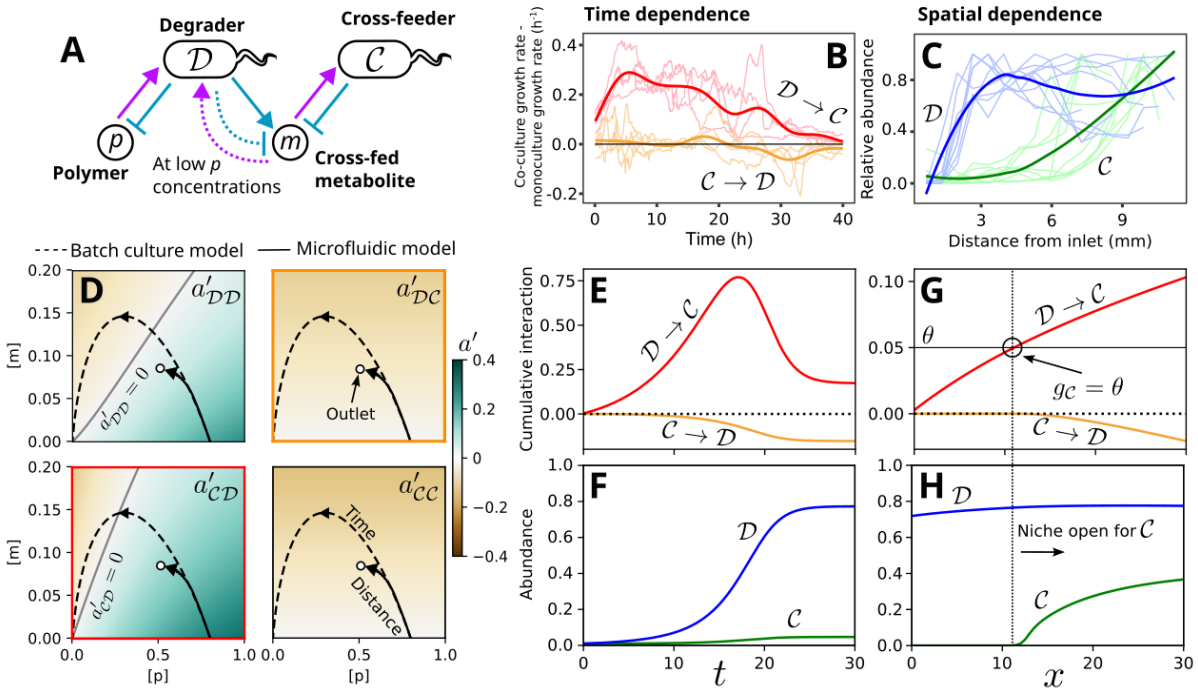

Figure 4: **Our framework shows that interaction time dependencies and spatial structure can arise from closely-related processes. A** Two recent studies[33,35] describe the ecological patterns arising in a two-species community consisting of a degrader $\mathcal{D}$ that consumes a polymer p and produces a metabolic by-product m which is consumed by a second crossfeeding species ($\mathcal{C}$). At low concentrations of p, $\mathcal{D}$ switches from net production of m to consumption. **B** Daniels et al.[33] find that this type of community displays time-dependent inter-specific interactions in batch culture, with the impact of $\mathcal{D}$ on $\mathcal{C}$ increasing early on and decreasing later (red) and the impact of $\mathcal{C}$ on $\mathcal{D}$ switching from neutral to negative (orange). **C** By contrast, Wong et al.[35] show how a similar community patterns itself in microfluidic channels with unidirectional flow, with $\mathcal{C}$ only being able to grow towards the outlet of the device. **D** We constructed an EO model of this community and applied our analytical techniques to obtain the instantaneous interaction matrix for each possible pair of community members (main text, methods). We then simulated the environmental trajectories of batch culture (dashed lines) and the microfluidic device (solid lines) inoculated with this community (methods). In the case of the microfluidic device, the initial environment $[p]_0, [m]_0$ corresponds to the composition of the media injected into the system at the inlet, while points along the environmental trajectory indicate the steady-state media composition at different positions along the channel. **E**, **F** In the batch-culture model, the gradual enhancement of the environment by $\mathcal{D}$ for $\mathcal{C}$ via conversion of p to m results in a gradual increase in the cumulative interaction from $\mathcal{D}$ to $\mathcal{C}$. Later, once p has been largely exhausted, the switch in the behaviour of $\mathcal{D}$ from net production to net uptake of m leads to competition between the two species, and a downward trend in both inter-specific cumulative interactions (**E**). These dynamics are difficult to dissect from the raw growth curves (**F**). **G**, **H** When this community is placed into the spatial context of a simulated microfluidic channel, we observe a similar interaction pattern from the inlet to the outlet, with a positive interaction accumulating from $\mathcal{D}$ to $\mathcal{C}$. At a certain position, this positive cumulative interaction exceeds the mortality rate θ representing the flushing of cells by flow. Beyond this point, the net growth rate of $\mathcal{C}$ is positive, reflecting the opening of a niche for $\mathcal{C}$ (**G**). This leads to the spatial structuring of the two species observed in experiments (**H**).

8 Supplementary Notes

8.1 Supplementary Note 1: Derivation of the cEO equation

To obtain our expression for the per-capita growth rate of a species α in a closed Environment-Organism system (Eq. 3), we begin from our definitions of the impact and sensitivity functions (Eqs. 1 and 2). We assume that the system sweeps out some trajectory Γ in the environment space which can be parameterized by the variable τ. τ can be interpreted as representing the history of the system up to the current query time t. At $\tau = 0$, the system begins at an initial position $\boldsymbol{r}_0$ in the environment space, while at $\tau = t$ it has reached an end position $\boldsymbol{r}(t)$. We seek to express the per-capita growth rate at this query time.

By our definition of the sensitivity function, we have

$$\frac{1}{s_\alpha}\frac{ds_\alpha}{dt} = g_\alpha(\boldsymbol{r}). \tag{22}$$

From the gradient theorem, we can rewrite this as

$$g_\alpha(\boldsymbol{r}) = g_\alpha(\boldsymbol{r}_0) + \int_\Gamma \nabla g_\alpha(\boldsymbol{r}) \cdot d\boldsymbol{r}, \tag{23}$$

where the second term is the path integral of the gradient of the sensitivity function over the trajectory Γ. We can use the definition of a path integral over a vector field to express this as

$$\begin{aligned}
\int_\Gamma \nabla g_\alpha(\boldsymbol{r}) \cdot d\boldsymbol{r} &= \int_0^t \nabla g_\alpha(\boldsymbol{r}) \cdot \frac{d\boldsymbol{r}}{d\tau} d\tau \\
&= \int_0^t \nabla g_\alpha(\boldsymbol{r}) \cdot \left(\boldsymbol{\sigma} + \sum_\beta \boldsymbol{f}_\beta(\boldsymbol{r})\, s_\beta \right) d\tau \\
&= \int_0^t \nabla g_\alpha(\boldsymbol{r}) \cdot \boldsymbol{\sigma}\, d\tau + \sum_\beta \int_0^t \nabla g_\alpha(\boldsymbol{r}) \cdot \boldsymbol{f}_\beta(\boldsymbol{r})\, s_\beta\, d\tau.
\end{aligned} \tag{24}$$

We find the term $\nabla g_\alpha(\boldsymbol{r}) \cdot \boldsymbol{f}_\beta(\boldsymbol{r})$ naturally arising in this expression. Calling this $a'_{\alpha\beta}(\boldsymbol{r})$, we can put together our final expression for open ecosystems:

$$\frac{1}{s_\alpha}\frac{ds_\alpha}{dt} = g_\alpha(\boldsymbol{r}_0) + \int_0^t \nabla g_\alpha(\boldsymbol{r}) \cdot \boldsymbol{\sigma}\ d\tau + \sum_\beta \int_0^t a'_{\alpha\beta}(\boldsymbol{r})\ s_\beta\ d\tau. \tag{25}$$

For closed systems, we can assume that $\boldsymbol{\sigma} = \mathbf{0}$, thus we obtain the cEO equation:

$$\frac{1}{s_\alpha}\frac{ds_\alpha}{dt} = g_\alpha(\boldsymbol{r}_0) + \sum_\beta \int_0^t a'_{\alpha\beta}(\boldsymbol{r})\ s_\beta\ d\tau. \tag{26}$$

8.2 Supplementary Note 2: Use of the EO framework to model systems under flow

In using our EO framework to simulate the dynamics of systems subject to flow, we need to be careful to specify the conditions under which our closed-system assumption ($\boldsymbol{\sigma} = 0$) holds true. Indeed, by having an inlet into which fresh nutrients can be continuously fed, this assumption would seem to be grossly violated by such systems. However, we can consider a fluid parcel travelling along the length of the system to behave as a closed system (in the sense that changes to its composition are only mediated by the local microbial populations at position x) as long as the rate of flow is large relative to the diffusion rate of intermediates.

We can show this formally by beginning with the 1D advection-diffusion equation used to specify the evolution of the distribution of intermediates along the system over time (Eq. 18):

$$\frac{\partial \boldsymbol{r}(x,t)}{\partial t} = D\frac{\partial^2 \boldsymbol{r}(x,t)}{\partial x^2} - v_x\frac{\partial \boldsymbol{r}(x,t)}{\partial x} + R. \tag{27}$$

We proceed by making two assumptions: firstly, we assume that the system reaches a steady-state concentration profile $\boldsymbol{r}^*(x)$ (associated with a static distribution of species $\boldsymbol{s}^*(x)$), allowing us to set this equation to zero. Secondly, we assume that the Péclet number Pe, which is defined as the ratio of the advective to diffusive transport rates, is substantially greater than 1. This allows us to neglect the diffusive term in the advection-diffusion equation. We therefore obtain

$$v_x\frac{d\boldsymbol{r}^*(x)}{dx} = R = \sum_\beta s^*_\beta(x)\boldsymbol{f}_\beta(\boldsymbol{r}^*(x)). \tag{28}$$

We note the similarity of this expression to our original definition of the rate of change of the environment in a batch culture system (Eq. 1). We can match these two expressions exactly by noting that $v_x = \frac{dx}{dt}$ and reparameterising the environmental trajectory $\boldsymbol{r}^*(x)$ in terms of the time coordinate of a fluid parcel relative to the time of its emergence at the inlet ($x = 0$). We can use this same reparameterisation to write Eq. 2 in terms of the steady-state concentration profile as traversed by the fluid parcel. These can finally be combined together to obtain a spatial version of Eq. 3, and a corresponding definition of the cumulative interaction (Methods). Thus, as long as we can justify the two original assumptions, our framework should be directly

applicable to such systems.

Beginning with the assumption that the system approaches a stationary distribution, we show in Fig S7 the environmental trajectories traced out along the length of the channel as a function of increasing simulated time. We observe, as expected, convergence on a static distribution $\boldsymbol{r}^*(t)$ over long timescales. It is difficult to define precise criteria under which this convergence will occur for general EO models, but a necessary condition is that the sensitivity functions g_α must contain a negative mortality term against which positive growth rates can be balanced in the long term. In our model, this is provided by θ, which describes the rate at which cells are washed off the surface of the channel by flow. An additional factor which we have found to be important is the inclusion of a density-dependent mechanism for capping growth at a particular spatial location, given in our case by the capacity λ. In the absence of this, species that are able to grow on the source media simply accumulate indefinitely at the inlet, rather than spreading out along the channel. Addition of these elements requires an adjustment to how the cumulative interaction is calculated, which we specify in the methods (section 6.1.4).

Now turning to Pe, we note that it is defined as $Pe = \frac{Lv_x}{D}$, where L is the characteristic length-scale of the system (in this case, the length of the channel). We can readily obtain approximate values for the diffusion constants of dextran and glucose (approximately 3×10^{-8} cm^2 s^{-1} and 5×10^{-6} cm^2 s^{-1}, respectively). Furthermore, in the experiments described in Wong et al.[35], $L = 2$ cm and v_x varied between 0.0003 cm s^{-1} and 0.003 cm s^{-1}. This gives us a range of Pe between 120 and 200,000, both substantially higher than 1 and firmly placing these experiments in the advection-dominated regime. We have also chosen the equivalent model parameters such that Pe varies between 75 and 1200, similarly placing the model in the advection-dominated regime.

9 Supplementary Figures

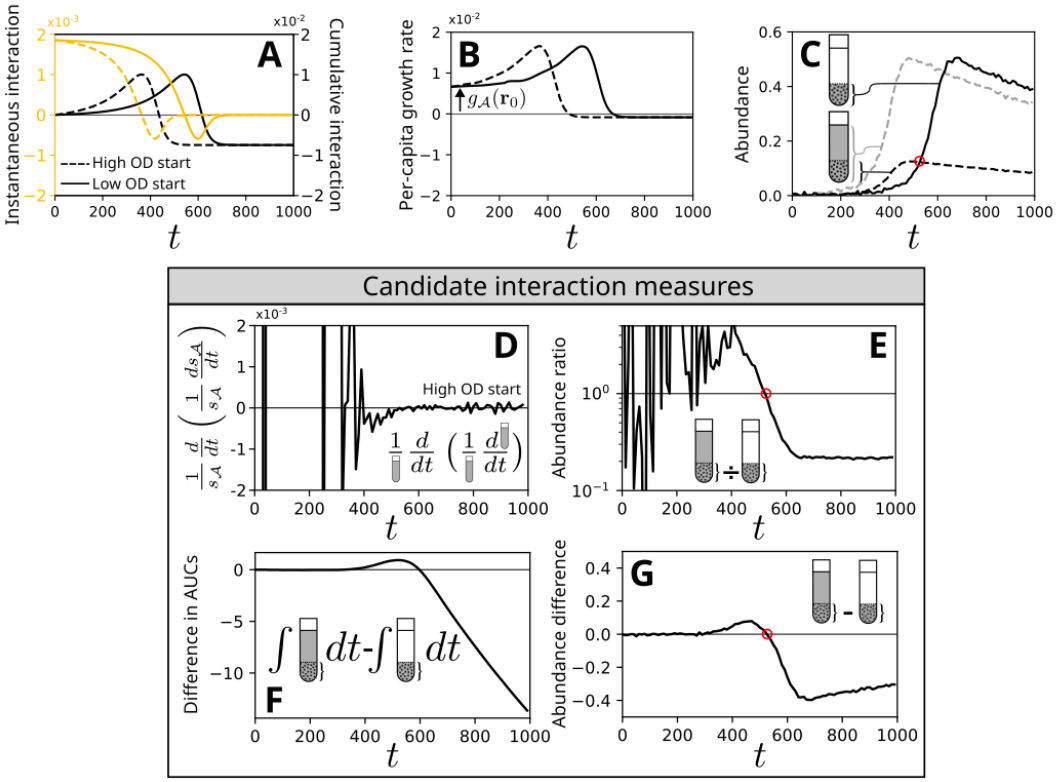

Figure S1: **Simulated batch cultures show abundance differences capture time-dependent interactions. A** We illustrate the relationship between the instantaneous, cumulative and measured intra-specific interactions for the toxin-nutrient system by simulating batch cultures initialised at high and low inoculation densities (compare Fig. 2F). **B** The per-capita growth rate of cells in each of these populations is given by adding a constant $g_{\mathcal{A}}(\boldsymbol{r}_0)$ – representing the growth rate of $\mathcal{A}$ in the initial environment $\boldsymbol{r}_0$ – to the cumulative interaction. **C** Integration of the per-capita growth rate yields growth curves for the two conditions. Here, normally distributed noise (s.d. = 0.005) has been added to simulate measurement noise. As in Fig. 3C, we measure the size of the sub-population in the high starting-density condition (black dashed line) matched to the low starting-density population (black solid line) by dividing the high-density growth curve (gray dashed line) by the ratio of inoculation densities. **D** One option to estimate interactions from these growth curves is to calculate the quantity $\frac{1}{s_{\mathcal{A}}}\frac{d}{dt}\left(\frac{1}{s_{\mathcal{A}}}\frac{ds_{\mathcal{A}}}{dt}\right)$ (shown for the high inoculation-density population), which from the cEO equation is expected to return the instantaneous intra-specific interaction for monocultures. **E** Alternatively, the ratio between the sub-populations over time indicates whether the sub-population in the high starting-density culture has grown more (positive interaction) or less (negative interaction) than that in the low starting-density culture.[9,10,41] While both of these approaches work in principle, in practice measurement noise is so strongly amplified at early time points when abundances are small that useful information cannot be reliably extracted. **F** The difference between the areas under the growth curves (AUCs) from the beginning of the experiment up to a query time is another alternative.[11,12] This captures the shape of the intra-specific interaction initially, but fails to stabilise once the cumulative interaction stops changing. **G** The abundance difference[13] displays low initial noisiness and long-term stability while also capturing the overall shape of the cumulative interaction, and is the primary experimental interaction measurement we use in this manuscript.

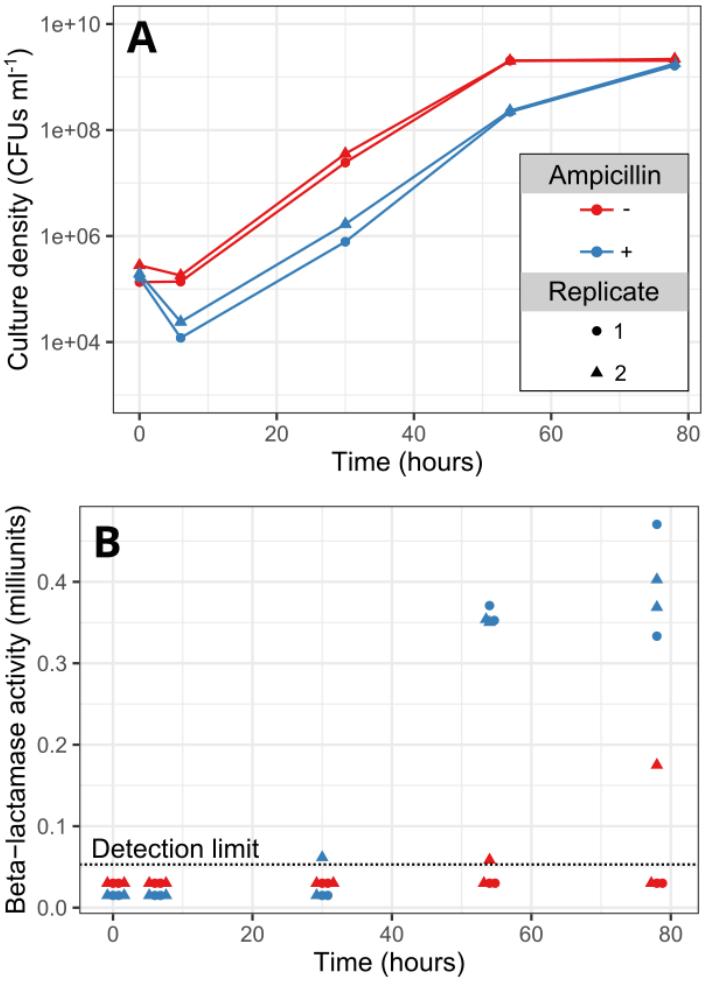

Figure S2: ***C. testosteroni* secretes β-lactamases when grown with ampicillin.** $n = 2$ cultures of *C. testosteroni* initialised from separate colonies were grown in media containing 5 mM proline and either with (blue) or without (red) ampicillin. Samples were taken from cultures at the indicated timepoints and cell densities (**A**) and β-lactamase activities (**B**) measured. One unit of β-lactamase is defined as the amount of enzyme needed to hydrolyse 1 nmol of nitrocefin in 1 ml of solution in 1 minute. Points with equal shapes and colours in **B** indicate $n = 2$ technical replicates of the β-lactamase assay performed on the same *C. testosteroni* culture at the same time.

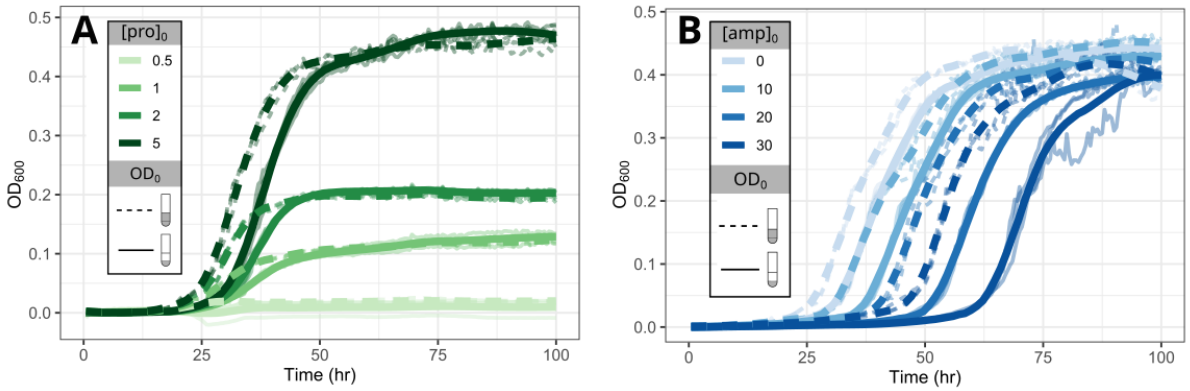

Figure S3: **Raw *C. testosteroni* growth curves under varying environmental conditions.** Raw growth curves (faint lines, $n = 3$ technical replicates for each condition) and cross-condition LOESS-smoothed averages (bold lines) for one biological replicate of the experiment shown in Fig. 3. Dashed lines indicate cultures inoculated at high OD, while solid lines indicate cultures inoculated at low OD. **A** All samples for which $[\text{amp}]_0 = 0$, representing the antibiotic-free control samples. **B** All samples for which $[\text{pro}]_0 = 5$mM.

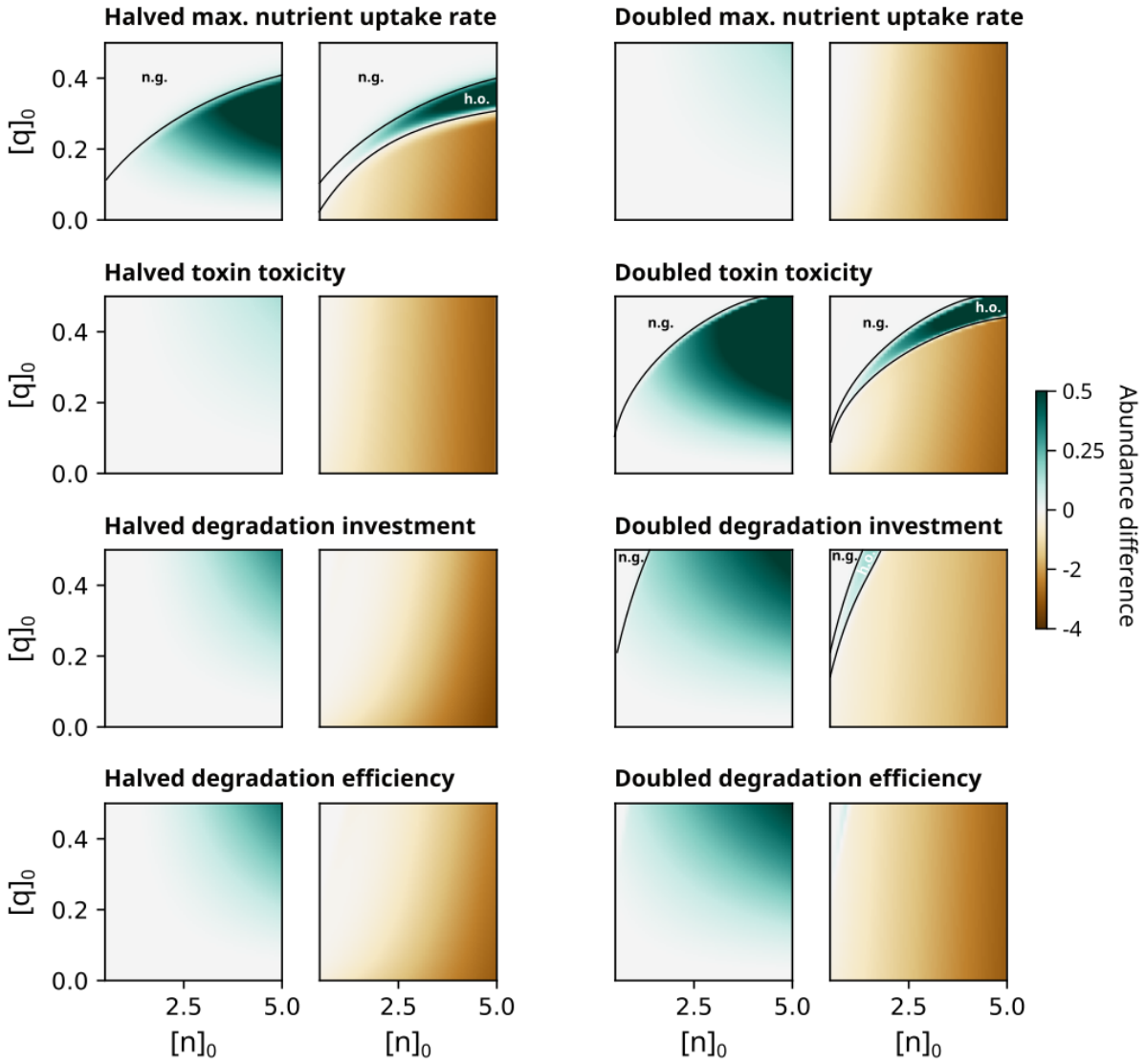

Figure S4: **Large shifts in the parameters of the toxin-nutrient model do not substantially impact the qualitative interaction patterns observed.** To investigate the robustness of the time-dependent interaction patterns observed in our toxin-nutrient model (Fig. 3H,I), we repeated our simulations with doubled and halved maximum nutrient uptake rate (ν_n, top), maximal toxin impact (ν_q, top-middle), toxin degradation investment (f, bottom-middle) and detoxification efficiency (δ, bottom). In the case of doubled ν_q and halved ν_n, we observe that in some environments with high toxin concentrations and low nutrient concentrations either only cells in the high inoculation OD conditions are able to grow (denoted 'h.o.') or that there is no growth for either inoculation density (denoted 'n.g.').

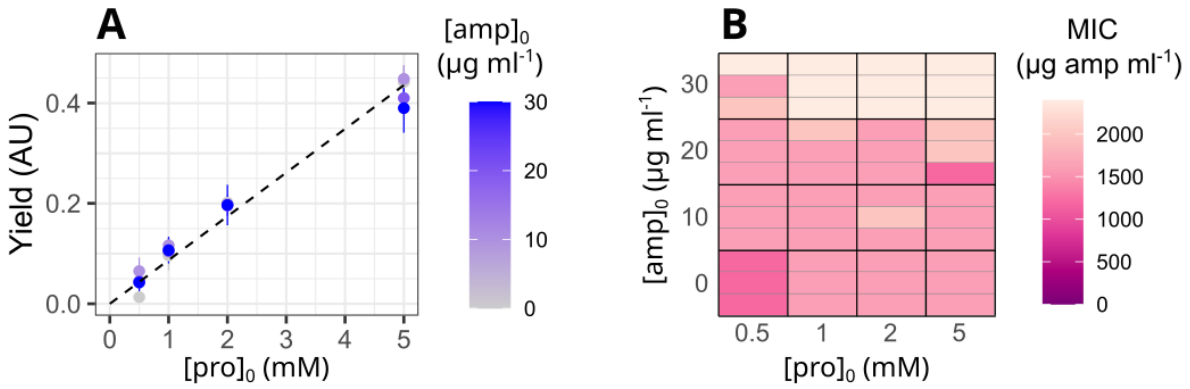

Figure S5: ***C. testosteroni* evolves stronger β-lactam resistance over experimental timescales.** Following one biological replicate of the experiment shown in Fig. 3, the minimum inhibitory concentration (MIC) of ampicillin was measured for each of the 48 low inoculation density wells (Methods). To prevent the inoculum effect from influencing our measurements,[38,39] we scaled the inoculation volume of culture by the concentration of proline in the environment. **A** This is directly proportional to the final yield of *C. testosteroni*, shown here as the OD measurement at 100 hours. This procedure thus ensured that the inoculated population size was approximately constant. **B** Heatmap showing the MIC of ampicillin measured for each environmental condition. For each condition, we show the result for each technical replicate as a separate horizontal strip.

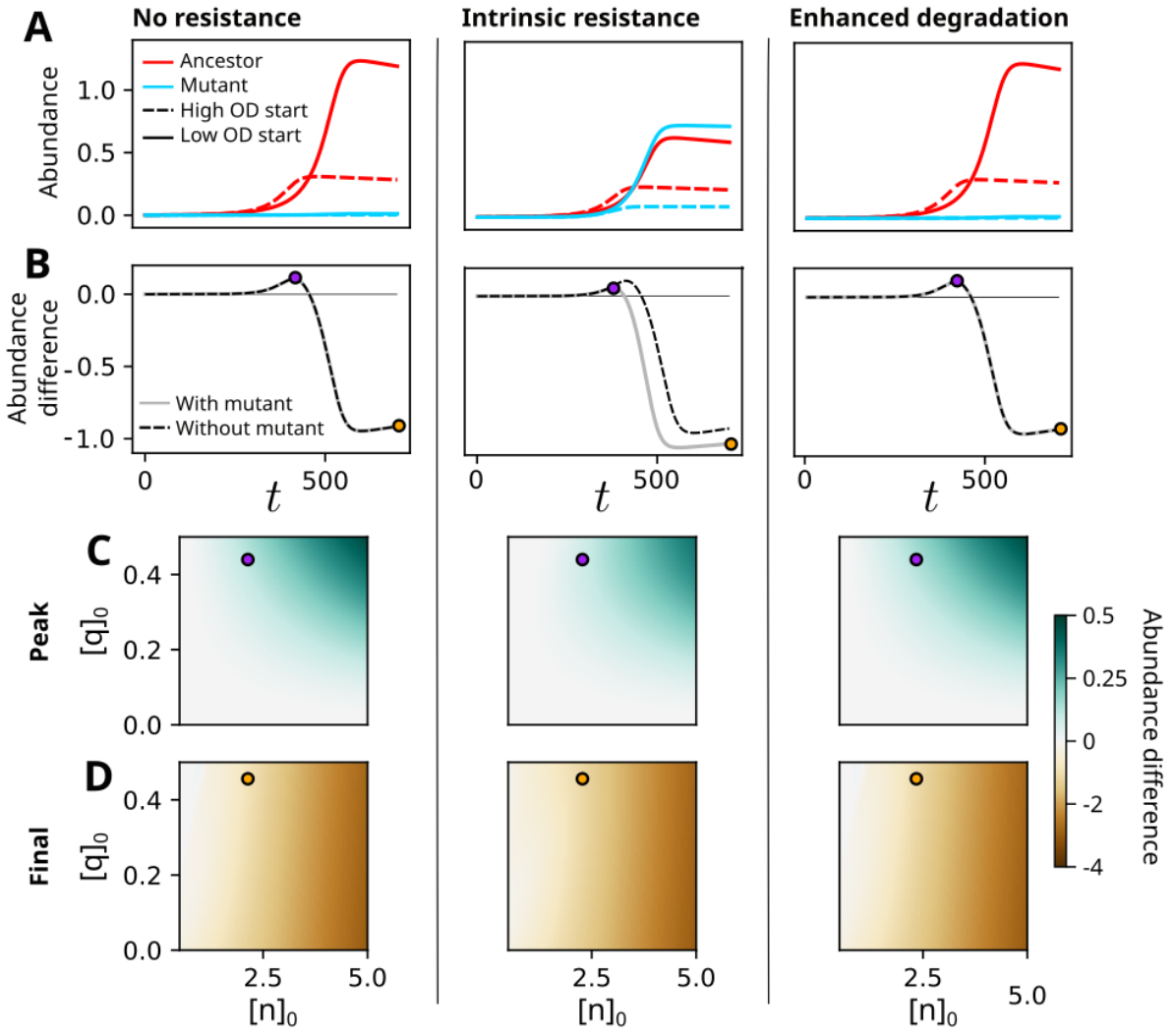

Figure S6: **Evolution of toxin resistance attenuates measured positive interaction strengths.** To investigate the effect of evolution of toxin resistance on interaction measurements in our toxin-nutrient system, we performed batch culture simulations in which an ancestral population was co-cultured with a small population (1 %) of mutant cells with either the same properties as the ancestral population (left), 5x stronger intrinsic resistance ($\nu_q/5$, middle) or 5x more efficient toxin degradation (5δ, right). **A** We show raw simulated abundance curves of the ancestral (red) and mutant (blue) populations when inoculated at high (dashed lines) and low (solid lines) densities. To assist comparisons, high inoculation density curves have been normalised by the inoculation ratio (compare Fig. 3B). **B** From these, we calculate time-dependent abundance differences between the total population sizes (sum of ancestral and mutant populations) in the high and low inoculation density conditions (grey lines, compare Fig. 3C). By comparing to a null model in which only the ancestral population is present (black dashed lines), we see that only the mutant with an increase in intrinsic resistance influences the measured interaction, weakly reducing the strength of the positive phase of the measurement. **C,D** This conclusion is supported by comparing the peak (C) and final (D) abundance differences across multiple environments (compare Fig. 3H,I). Purple and orange points indicate the initial environmental composition of the simulations shown in A and B.

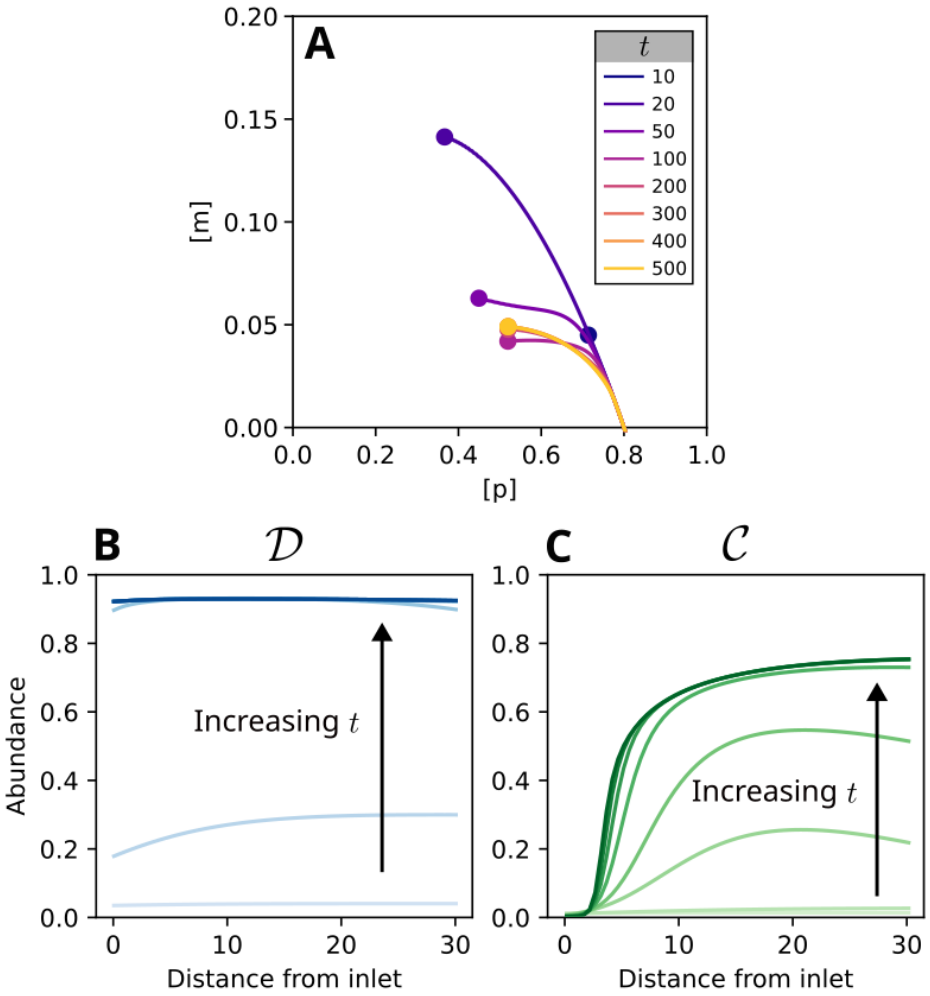

Figure S7: **Our spatial model of a microfluidic channel stabilises over long timescales.** An assumption necessary for our framework to be applied to spatially varying environments is that the composition of the environment is static (Supplementary Note 2). **A** To confirm this condition was met in our model of the microfluidic channel at long timescales, we plotted the trajectories representing the spatially-varying environment after different simulation lengths (t) when the flow velocity $v_x = 2.5$. These sweep out a curve from the position representing the inlet composition ($[p]_o = 0.8$, $[m]_o = 0$) to the composition at the outlet (circular points). After an initial transient during community establishment, we observe that the environmental trajectory traces out a consistent curve beyond $t = 200$. **B, C** This stabilisation of the environment corresponds to a stabilisation of the spatial structure of the community, as shown by the changing distribution of the degrader (**B**) and cross-feeder (**C**) along the length of the channel over time. Increasingly dark shades of blue and green in these plots indicate later sampling times of the simulation and correspond to the same sampling times in panel A. All other microfluidic simulations in this manuscript are sampled at $t = 1000$.

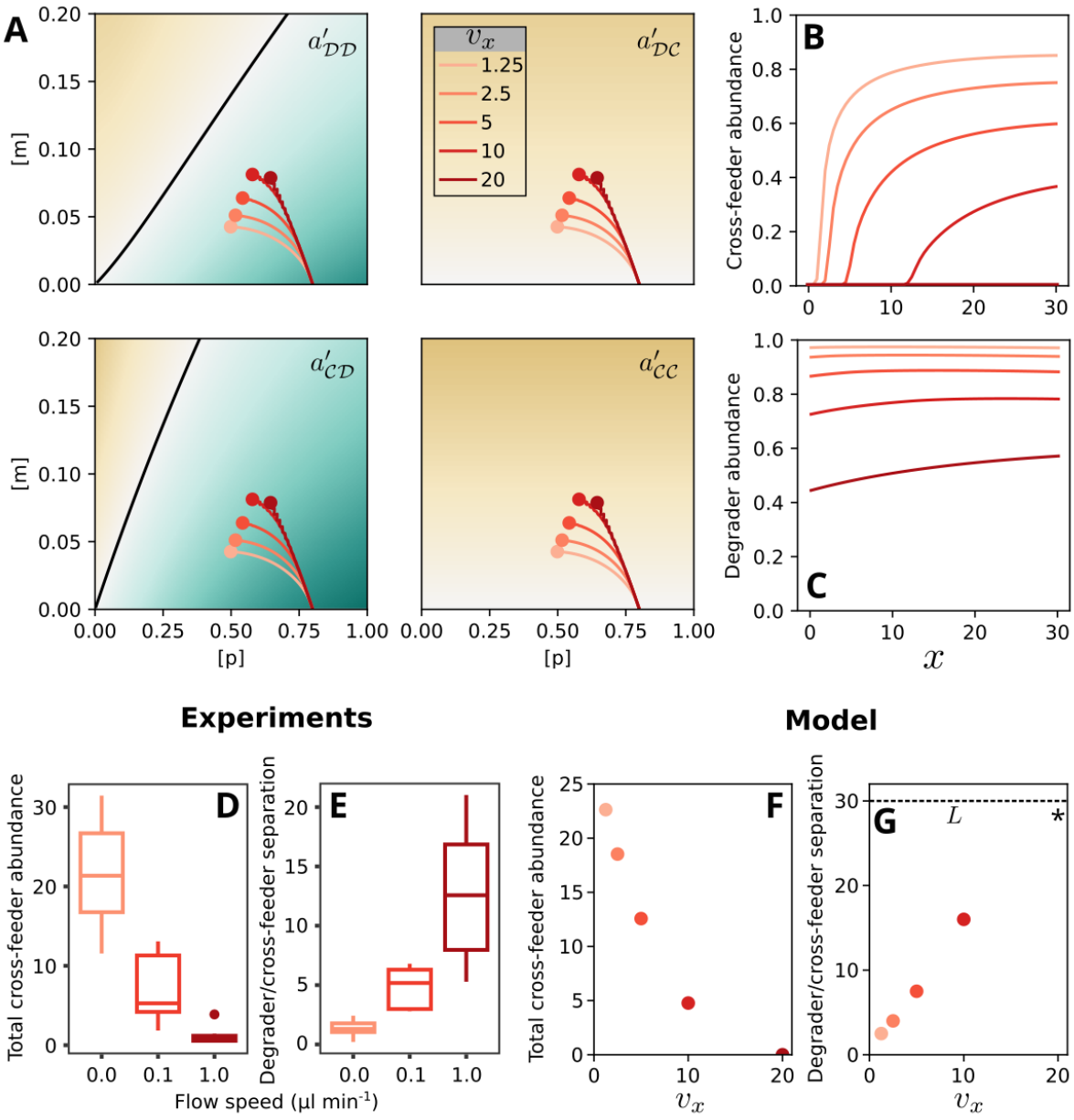

Figure S8: **Changes in the spatial structure of simulated microfluidic communities under varying flow speeds matche experimental observations. A** Variation of the flow speed v_x in simulated microfluidic channels results in different environmental trajectories swept out along the length of the system. Here we plot the resulting steady-state environmental trajectories on top of the instantaneous interaction maps for the degrader $\mathcal{D}$ and crossfeeder $\mathcal{C}$ species (Fig. 4D). These curves represent the variation in the composition of the environment from the inlet ($[p]_0 = 0.8$, $[m]_0 = 0$) to the outlet (circular points). **B, C** These different trajectories, combined with variations in the wash-out rate θ induced by different flow rates, result in different spatial structuring of the cross-feeder (**B**) and the degrader (**C**) along the length of the device. **D, E** The impact of flow rate on the total abundance of the cross-feeder (**D**, replotted from Wong et al.[35]) and the spatial separation between the the degrader and the cross-feeder growth zones (**E**, replotted from Wong et al.[35]) were previously quantified experimentally. **F, G** We evaluated these quantities from the steady-state species abundance profiles from our model, finding identical trends as in the experiments. The dashed line in **G** indicates the channel length L. As we do not observe growth of the crossfeeder in the highest flowrate simulation, we indicate that the separation between the degrader and crossfeeder growth zones is not defined for this simulation with an asterisk.

References

[1] Pringle, E. G. *PLOS Biology* **2016**, *14*, e2000891.

[2] Lidicker, W. Z. *BioScience* **1979**, *29*, 475–477.

[3] Allesina, S.; Tang, S. *Nature* **2012**, *483*, 205–208.

[4] Novak, M.; Yeakel, J. D.; Noble, A. E.; Doak, D. F.; Emmerson, M.; Estes, J. A.; Jacob, U.; Tinker, M. T.; Wootton, J. T. *Annual Review of Ecology, Evolution, and Systematics* **2016**, *47*, 409–432.

[5] Paine, R. T. *Nature* **1992**, *355*, 73–75.

[6] Gonze, D.; Coyte, K. Z.; Lahti, L.; Faust, K. *Current Opinion in Microbiology* **2018**, *44*, 41–49.

[7] van den Berg, N. I.; Machado, D.; Santos, S.; Rocha, I.; Chacón, J.; Harcombe, W.; Mitri, S.; Patil, K. R. *Nature Ecology and Evolution* **2022**, *6*, 855–865.

[8] Palmer, J. D.; Foster, K. R. *Science* **2022**, *376*, 581–582.

[9] Vos, M. G. D.; Zagorski, M.; McNally, A.; Bollenbach, T. *Proceedings of the National Academy of Sciences of the United States of America* **2017**, *114*, 10666–10671.

[10] Hsu, R. H.; Clark, R. L.; Tan, J. W.; Ahn, J. C.; Gupta, S.; Romero, P. A.; Venturelli, O. S. *Cell Systems* **2019**, *9*, 229–242.e4.

[11] Piccardi, P.; Vessman, B.; Mitri, S. *Proceedings of the National Academy of Sciences of the United States of America* **2019**, *116*, 15979–15984.

[12] Weiss, A. S. et al. *The ISME Journal 2021 16:4* **2021**, *16*, 1095–1109.

[13] Foster, K. R.; Bell, T. *Current Biology* **2012**, *22*, 1845–1850.

[14] Qian, Y.; Lan, F.; Venturelli, O. S. *Current Opinion in Microbiology* **2021**, *62*, 84–92.

[15] Picot, A.; Shibasaki, S.; Meacock, O. J.; Mitri, S. *Current Opinion in Microbiology* **2023**, *75*, 102354.

[16] Gralka, M.; Szabo, R.; Stocker, R.; Cordero, O. X. *Current Biology* **2020**, *30*, R1176–R1188.

[17] D'Souza, G.; Shitut, S.; Preussger, D.; Yousif, G.; Waschina, S.; Kost, C. *Natural Product Reports* **2018**, *35*, 455–488.

[18] Datta, M. S.; Sliwerska, E.; Gore, J.; Polz, M. F.; Cordero, O. X. *Nature Communications* **2016**, *7*, 11965.

[19] Granato, E. T.; Meiller-Legrand, T. A.; Foster, K. R. *Current Biology* **2019**, *29*, R521–R537.

[20] MacArthur, R. *Theoretical Population Biology* **1970**, *1*, 1–11.

[21] Tilman, D. *The American Naturalist* **1980**, *116*, 362–393.

[22] Koffel, T.; Daufresne, T.; Klausmeier, C. A. *Ecological Monographs* **2021**, *91*, e01458.

[23] Momeni, B.; Xie, L.; Shou, W. *eLife* **2017**, *6*.

[24] Chang, C.-Y.; Bajić, D.; Vila, J. C. C.; Estrela, S.; Sanchez, A. *Science* **2023**, *381*, 343–348.

[25] Friedman, J.; Higgins, L. M.; Gore, J. *Nature Ecology & Evolution* **2017**, *1*, 1–7.

[26] Dolinšek, J.; Goldschmidt, F.; Johnson, D. R. *FEMS Microbiology Reviews* **2016**, *40*, 961–979.

[27] Klitgord, N.; Segrè, D. *PLOS Computational Biology* **2010**, *6*, e1001002.

[28] Hoek, T. A.; Axelrod, K.; Biancalani, T.; Yurtsev, E. A.; Liu, J.; Gore, J. *PLOS Biology* **2016**, *14*, e1002540.

[29] Hammarlund, S. P.; Chacón, J. M.; Harcombe, W. R. *Environmental Microbiology* **2019**, *21*, 759–771.

[30] Di Martino, R.; Picot, A.; Mitri, S. *bioRxiv* **2023**, 2023.05.24.542164.

[31] Rodríguez-Verdugo, A.; Vulin, C.; Ackermann, M. *Ecology Letters* **2019**, *22*, 838–846.

[32] Venkataram, S.; Kuo, H.-Y.; Hom, E. F. Y.; Kryazhimskiy, S. *Nature Ecology and Evolution* **2023**, *7*, 143–154.

[33] Daniels, M.; van Vliet, S.; Ackermann, M. *The ISME Journal 2023* **2023**, 1–11.

[34] Nadell, C. D.; Drescher, K.; Foster, K. R. *Nature Reviews Microbiology* **2016**, *14*, 589–600.

[35] Wong, J. P. H.; Fischer-Stettler, M.; Zeeman, S. C.; Battin, T. J.; Persat, A. *Proceedings of the National Academy of Sciences* **2023**, *120*, e2217577120.

[36] Meszéna, G.; Gyllenberg, M.; Pásztor, L.; Metz, J. A. *Theoretical Population Biology* **2006**, *69*, 68–87.

[37] Estrela, S.; Libby, E.; Cleve, J. V.; Débarre, F.; Deforet, M.; Harcombe, W. R.; Peña, J.; Brown, S. P.; Hochberg, M. E. *Trends in Ecology and Evolution* **2019**, *34*, 6–18.

[38] Parker, R. F. *Experimental Biology and Medicine* **1946**, *63*, 443–446.

[39] Lenhard, J. R.; Bulman, Z. P. *Journal of Antimicrobial Chemotherapy* **2019**, *74*, 2825–2843.

[40] Mitri, S.; Richard Foster, K. *Annual Review of Genetics* **2013**, *47*, 247–273, PMID: 24016192.

[41] Kehe, J.; Ortiz, A.; Kulesa, A.; Gore, J.; Blainey, P. C.; Friedman, J. *Science Advances* **2021**, *7*, 7159.

[42] Orr, H. A.; Unckless, R. L. *PLOS Genetics* **2014**, *10*, e1004551.

[43] Ramsayer, J.; Kaltz, O.; Hochberg, M. E. *Evolutionary Applications* **2013**, *6*, 608–616.

[44] Agrawal, A. A. et al. *Frontiers in Ecology and the Environment* **2007**, *5*, 145–152.

[45] Bronstein, J. L. *Trends in Ecology and Evolution* **1994**, *9*, 214–217.

[46] Catford, J. A.; Wilson, J. R. U.; Pyšek, P.; Hulme, P. E.; Duncan, R. P. *Trends in Ecology and Evolution* **2022**, *37*, 158–170.

[47] Hernandez, M. J. *Proceedings of the Royal Society B: Biological Sciences* **1998**, *265*, 1433–1440.

[48] Holland, J. N.; Deangelis, D. L. *Ecology Letters* **2009**, *12*, 1357–1366.

[49] O'Dwyer, J. P. *Theoretical Ecology* **2018**, *11*, 441–452.

[50] Goldford, J. E.; Lu, N.; Bajić, D.; Estrela, S.; Tikhonov, M.; Sanchez-Gorostiaga, A.; Segrè, D.; Mehta, P.; Sanchez, A. *Science* **2018**, *361*, 469–474.

[51] Müller, M. J. I.; Neugeboren, B. I.; Nelson, D. R.; Murray, A. W. *Proceedings of the National Academy of Sciences of the United States of America* **2014**, *111*, 1037–1042.

[52] Yu, J. S. et al. *Nature Microbiology* **2022**, *7*, 542–555.

[53] Zelezniak, A.; Andrejev, S.; Ponomarova, O.; Mende, D. R.; Bork, P.; Patil, K. R. *Proceedings of the National Academy of Sciences of the United States of America* **2015**, *112*, 6449–6454.

[54] Roberts, D. W. *Vegetatio* **1987**, *69*, 27–33.

[55] Smith, C. R.; Glover, A. G.; Treude, T.; Higgs, N. D.; Amon, D. J. *Annual Review of Marine Science* **2015**, *7*, 571–596.

[56] Pontrelli, S.; Szabo, R.; Pollak, S.; Schwartzman, J.; Ledezma-Tejeida, D.; Cordero, O. X.; Sauer, U. *Science Advances* **2022**, *8*, eabk3076.

[57] Vannote, R. L.; Minshall, G. W.; Cummins, K. W.; Sedell, J. R.; Cushing, C. E. *Canadian Journal of Fisheries and Aquatic Sciences* **1980**, *37*, 130–137.

[58] Riva, A.; Kuzyk, O.; Forsberg, E.; Siuzdak, G.; Pfann, C.; Herbold, C.; Daims, H.; Loy, A.; Warth, B.; Berry, D. *Nature Communications* **2019**, *10*, 1–11.

[59] Pereira, F. C.; Berry, D. *Environmental Microbiology* **2017**, *19*, 1366–1378.

[60] Sanchez, A. *Cell Systems* **2019**, *9*, 519–520.

[61] Billick, I.; Case, T. J. *Ecology* **1994**, *75*, 1529–1543.

[62] Letten, A. D.; Stouffer, D. B. *Ecology Letters* **2019**, *22*, 423–436.

[63] Abrams, P. A. *The American Naturalist* **1983**, *121*, 887–891.

[64] Mickalide, H.; Kuehn, S. *Cell Systems* **2019**, *9*, 521–533.e10.

[65] Smith, H. L.; Waltman, P. *The Theory of the Chemostat: Dynamics of Microbial Competition*; Cambridge University Press, 1995.

[66] Sockett, R. E. *Annual Review of Microbiology* **2009**, *63*, 523–539.

[67] Hayes, C. S.; Aoki, S. K.; Low, D. A. *Annual Review of Genetics* **2010**, *44*, 71–90.

[68] Drescher, K.; Nadell, C. D.; Stone, H. A.; Wingreen, N. S.; Bassler, B. L. *Current Biology* **2014**, *24*, 50–55.

[69] Sulheim, S.; Mitri, S. *Trends in Microbiology* **2023**, *31*, 426–427.

[70] Kim, J.; Kim, H.-S.; Han, S.; Lee, J.-Y.; Oh, J.-E.; Chung, S.; Park, H.-D. *Lab on a Chip* **2013**, *13*, 1846–1849.